land

MDPI

Article

Multi-Decadal Land Subsidence Risk Assessment at Major Italian Cities by Integrating PSInSAR with Urban Vulnerability

Michelle Lenardón Sánchez [1,2], Celina Anael Farías [1,2] and Francesca Cigna [1,*]

[1] Institute of Atmospheric Sciences and Climate (ISAC), National Research Council (CNR), Via del Fosso del Cavaliere 100, 00133 Rome, Italy; michelle.lenardon@mi.unc.edu.ar (M.L.S.); celina.farias@mi.unc.edu.ar (C.A.F.)

[2] Faculty of Exact, Physics and Natural Sciences, Nacional University of Córdoba (UNC), Av. Vélez Sarsfield 299, Córdoba X5000 JJC, Argentina

* Correspondence: f.cigna@isac.cnr.it

Abstract: This study assesses subsidence-induced risk to urban infrastructure in three major Italian cities—Rome, Bologna, and Florence—by integrating satellite-based persistent scatterer interferometric synthetic aperture radar (PSInSAR) ground displacement data with urban vulnerability metrics into a novel risk assessment workflow, incorporating land use and population data from the Copernicus Land Monitoring Service (CLMS)—Urban Atlas. This analysis exploits ERS-1/2, ENVISAT, and COSMO-SkyMed PSInSAR datasets from the Italian Extraordinary Plan of Environmental Remote Sensing, plus Sentinel-1 datasets from CLMS—European Ground Motion Service (EGMS), and spans a 30-year period, thus capturing both historical and recent subsidence trends. Angular distortion is introduced as a critical parameter for assessing potential structural damage due to differential settlement, which helps to quantify subsidence-induced hazards more precisely. The results reveal variable subsidence hazard patterns across the three cities, with specific areas exhibiting significant differential ground deformation that poses risks to key infrastructure. A total of 36.15, 11.44, and 0.43 km^2 of land at high to very high risk are identified in Rome, Bologna, and Florence, respectively. By integrating geospatial and vulnerability data at the building-block level, this study offers a more comprehensive understanding of subsidence-induced risk, potentially contributing to improved management and mitigation strategies in urban areas. This study contributes to the limited literature on embedding PSInSAR data into urban risk assessment workflows and provides a replicable framework for future applications in other urban areas.

Keywords: subsidence; InSAR; persistent scatterer interferometry (PSI); EGMS; PST-A; geological hazards; risk assessment; Copernicus Urban Atlas

Citation: Lenardón Sánchez, M.; Farías, C.A.; Cigna, F. Multi-Decadal Land Subsidence Risk Assessment at Major Italian Cities by Integrating PSInSAR with Urban Vulnerability. *Land* **2024**, *13*, 2103. https://doi.org/10.3390/land13122103

Academic Editor: Faccini Francesco

Received: 24 October 2024
Revised: 24 November 2024
Accepted: 2 December 2024
Published: 5 December 2024

1. Introduction

Geological risk mapping plays a vital role in understanding and managing the impact of hazards on urban environments. In this context, it is important to clarify the distinction between hazard and risk: hazard refers to a potentially damaging phenomenon, while risk is the likelihood of the hazard occurring combined with the exposure of people, infrastructure, or ecosystems and their vulnerability to its impacts [1]. As [2] noted, risk mitigation can be successful only when detailed knowledge is obtained about the frequency, character, and magnitude of hazardous events in an area, data which have a strong geographic component. Geological risk mapping involves the spatial identification and assessment of areas prone to geological hazards, such as landslides, earthquakes, or land subsidence, which can threaten infrastructure and human safety.

Among these hazards, land subsidence—the gradual lowering of the Earth's surface—stands out as a significant issue in many metropolitan regions globally [3]. Subsidence can result from both natural processes, such as the compaction of sedimentary layers [4] and human activities, including groundwater extraction [5–7] and urban development [8,9]. Its

consequences are often severe, leading to structural damage, ground instability, and increased susceptibility to flooding [10,11]. Given the potential scale of its impact, the accurate and continuous monitoring of subsidence is essential for risk mapping and mitigation, particularly in rapidly expanding cities.

In recent years, satellite-based differential interferometric synthetic aperture radar (DInSAR) techniques have emerged as a precise method for estimating ground displacements associated with geological processes [12] and, among them, land subsidence [13]. DInSAR allows for high-resolution, large-scale observation of the displacement of the Earth's surface with up to millimeter-level accuracy [14,15]. Despite the demonstrated technical performance and widespread application of DInSAR for subsidence monitoring, there is still limited literature addressing its integration into comprehensive risk assessment frameworks, especially concerning urban infrastructure. In this context, recent advancements as key studies on major metropolises of Central Mexico, Nigeria, and India have started to address this gap. A novel subsidence-induced risk assessment approach applied to Mexico City, Aguascalientes, and Morelia has been developed to integrate InSAR-derived data with geospatial and socioeconomic factors [9,16,17]. Other scholars further modified this methodology for application in Lagos [18] and National Capital Region (Delhi) [19], demonstrating its adaptability across different geographical contexts. These approaches underscore the potential for InSAR to contribute to more robust subsidence risk mapping and monitoring strategies, when coupled with detailed vulnerability assessments.

Building upon these recent developments, this study innovates in the field by attempting, for the first time, a multi-decadal risk assessment by integrating several persistent scatterer InSAR (PSInSAR) datasets covering an overall period of 30 years, to assess land subsidence and its temporal evolution in three major cities in Italy: Rome, Bologna, and Florence. The existing methodology is also further enhanced by incorporating land use and population data from the Copernicus Urban Atlas at the building-block level, and, therefore, detailing the risk assessment at the scale of single urban blocks and providing a more detailed evaluation of urban infrastructure vulnerability and, in turn, risk. This comprehensive approach aims to enhance the precision of subsidence-induced risk assessments, contributing to more effective management and mitigation strategies in urban areas.

2. Study Areas

Three major cities in Italy were used to test and demonstrate the novel subsidence-induced risk assessment workflow: Rome, Bologna, and Florence. These cities were selected due to their significance in terms of urban infrastructure, cultural heritage, and their assorted susceptibility to subsidence, thus allowing a comprehensive understanding of subsidence hazards in different geological and urban contexts.

Rome, the capital of Italy and the Lazio region, not only is a historical and cultural epicenter but also is one of the world's most visited cities, with nearly 3 million residents spread across 1287 km^2. Strategically situated along the Tiber River, the city lies within the Tiber's lower valley, bordered by low hills and extending toward the Tyrrhenian Sea. The landscape includes the Colli Albani foothills to the southeast, the Sabatini Mountains to the northwest, and the Central Apennines at the northeast (Figure 1a). Geologically, the region features a mix of volcanic activity and fluvial processes. According to [20], volcanic deposits, particularly pyroclastic tuff from the Albano and Sabatino volcanic districts, dominate the area, while alluvial sediments have accumulated in the Tiber Valley between these districts. The Tiber River's hydrographic network, shaped by Pleistocene sea-level changes, has led to the formation of alluvial plains, underlain by fine-grained soils prone to settling due to urban development activities. This process led to the formation of the extensive alluvial plains that the city has expanded upon. Recent sediment deposits in these incisions consist of fine-grained soils, which are susceptible to settling due to urban activities such as leveling the ground, infrastructure construction (e.g., buildings), and variations in groundwater levels [21].

Bologna is the seventh most populous city in Italy, with ~400 thousand inhabitants on an administrative area of 140.9 km^2. It is located in the Emilia-Romagna Region at the Apennines foothill, along the southern boundary of the Po River sedimentary basin (Po Plain). It is bounded to the west and east by the Reno and Savena rivers, respectively (Figure 1b). The geological and morphological setting, influenced by the alluvial fans of these rivers, primarily consists of stacked coarse-grained deposits, as described by [22]. The deposits gradually transition into less consolidated and finer sediment bodies toward their distal portions, making them more vulnerable to the rearrangement of particles when the natural equilibrium is modified, which results in surface deformations. These aquifer deposits have been subject to excessive groundwater pumping since the 1950s, resulting in peak subsidence rates of 110 mm/year during the 1970s and 1980s [23]. As discussed in [23], subsequent to the implementation of regional water pumping restrictions, starting in the 1980s, this phenomenon began to decline.

Florence is a city that is constantly expanding. The administrative area corresponds to 102 km^2 with ~388 thousands of permanent inhabitants. The city lies on the southeast corner of the Florence–Prato–Pistoia plain, which appears as an elongated depression with a northwest–southeast direction (Figure 1c). It is surrounded by reliefs and the Arno River runs through it. Florence is immersed in a charming landscape that is a consequence of the geotectonic evolution of the Northern Apennines over the last million years (Pliocene to present). This resulted in three unconformable boundary stratigraphic units: fluvial–lacustrine deposits, ancient alluvial deposits, and recent alluvial deposits.

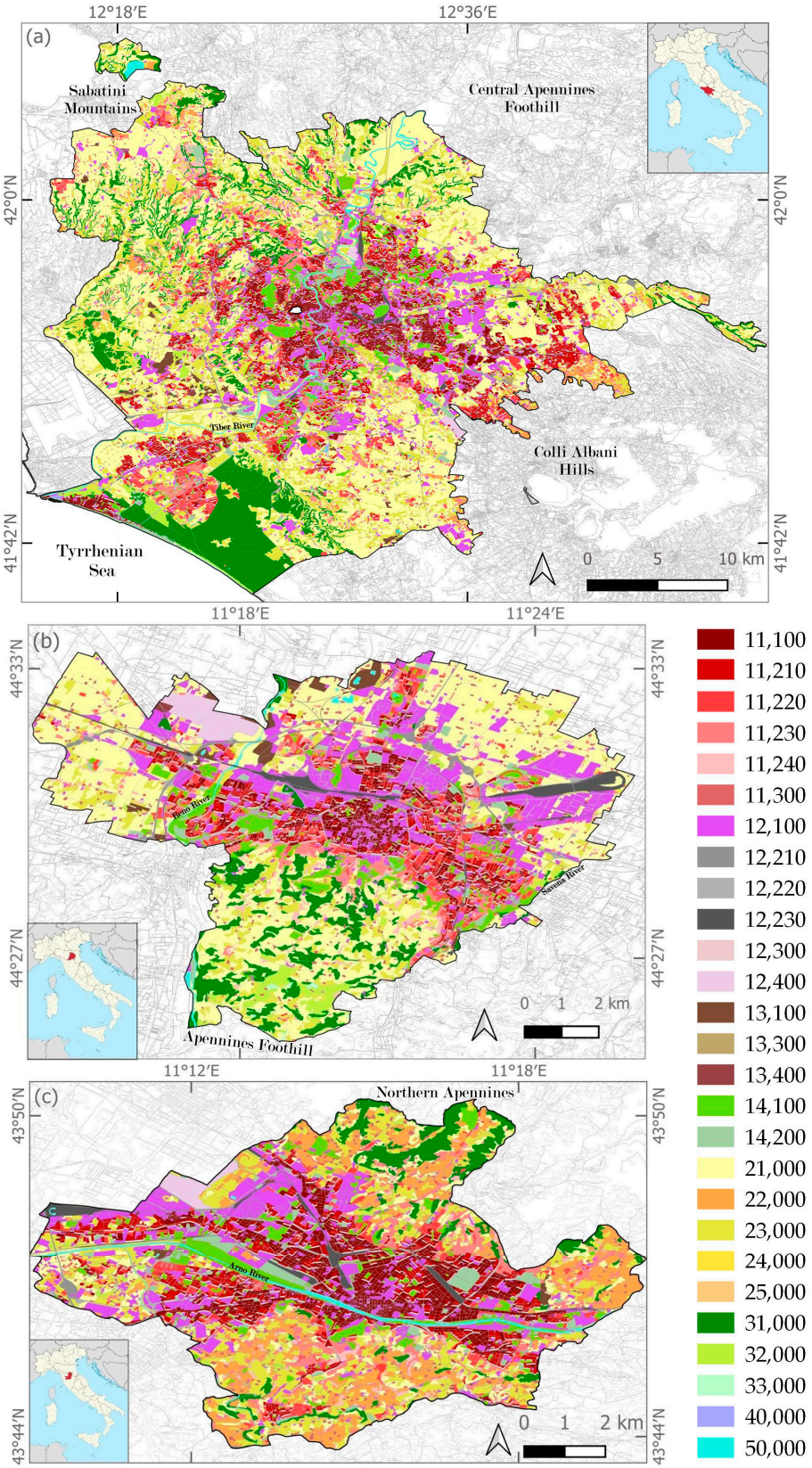

Figure 1. Location and land use/cover of the cities of (**a**) Rome; (**b**) Bologna, and (**c**) Florence in Italy, according to the Copernicus Urban Atlas (UA) 2018 dataset [24]. Land use/cover types associated with UA codes are provided in Table 1.

Table 1. Urban Atlas Land Cover/Land Use 2018 classes and associated codes, with the exposure-vulnerability scores assigned for the subsidence-induced risk analysis (see Section 4.3): 1, low; 2, medium; 3, high; 4, very high. Notation: S.L., sealing level; NA, not applicable.

Urban Atlas Class	Code	Score
Continuous urban fabric (S.L.: >80%)	11,100	4
Discontinuous dense urban fabric (S.L.: 50–80%)	11,210	4
Discontinuous medium-density urban fabric (S.L.: 30–50%)	11,220	3
Discontinuous low-density urban fabric (S.L.: 10–30%)	11,230	2
Discontinuous very low-density urban fabric (S.L.: <10%)	11,240	2
Isolated Structures	11,300	1
Industrial, commercial, public, military, and private units	12,100	3
Fast transit roads and associated land	12,210	4
Other roads and associated land	12,220	3
Railways and associated land	12,230	4
Airports	12,400	4
Mineral extraction and dump sites	13,100	3
Construction sites	13,300	2
Land without current use	13,400	1
Green Urban Areas	14,100	1
Sports and leisure facilities	14,200	2
Arable land (annual crops)	21,000	1
Permanent crops (vineyards, fruit trees, olive groves)	22,000	1
Pastures	23,000	1
Forests	31,000	1
Herbaceous vegetation associations (natural grassland, moors)	32,000	1
Open spaces with little or no vegetation (beaches, dunes, rocks)	33,000	1
Wetlands	40,000	NA
Water	50,000	NA

3. Data

To account for the elements at risk in the analysis, openly available land use/cover data from Copernicus Land Monitoring Service (CLMS) were used. In particular, the most updated release (2018) of the Urban Atlas (UA) Land Cover/Land Use (LCLU) was exploited [25]. This provides reliable, inter-comparable, very high-resolution land use and land cover data with integrated population estimates in INSPIRE-compliant vector format for the functional urban areas (FUA) of Europe with more than 50,000 inhabitants, with a new release every 6 years. The adopted LCLU nomenclature includes 17 urban classes with a minimum mapping unit of 0.25 ha, and 10 rural classes with a minimum mapping unit of 1 ha (see Table 1). The mapping is based on the interpretation of very high-resolution satellite imagery (e.g., Pléiades, KOMPSAT, Planet, SPOT-6, and SuperView) supported by Google Earth and OpenStreet Map ancillary data [25], and the resulting minimum mapping width is 10 m [26]. The LCLU 2018 product was accessed for the whole FUAs of Rome, Bologna, and Florence, and then clipped to the administrative areas of the three cities.

To conduct a comprehensive analysis of the ground vertical displacement in each study area, two sources of InSAR datasets were employed: (i) ERS-1/2, ENVISAT, and COSMO-SkyMed ascending and descending mode datasets provided by the Extraordinary Plan of Environmental Remote Sensing (Piano Straordinario di Telerilevamento Ambientale, PST-A) [27] of the Italian Ministry of the Environment and Energy Security, and (ii) Sentinel-1 ascending and descending mode datasets from CLMS—European Ground Motion Service [26] (Table 2). The products consist of long data-stacks of satellite SAR images processed with persistent scatterer interferometry (PSI) algorithms (also commonly indicated with PSInSAR) to identify good radar reflectors, called permanent/persistent scatterers (PS), the displacement of which can be monitored accurately over long time intervals [27].

Table 2. Main characteristics of the satellite PSInSAR datasets used for the analysis of subsidence-induced hazards in the three study areas.

Study Area	Satellite	Orbit Type	Time Interval	LOS Velocity [mm/year]	
				Minimum	Maximum
Rome	ERS-1/2	Ascending	April 1993–November 2000	–34.8	+15.0
		Descending	September 1992–December2000	–42.7	+28.6
	ENVISAT	Ascending	November 2002–July 2010	–33.1	+6.8
		Descending	January 2003–June 2010	–30.7	+6.8
	COSMO-SkyMed	Ascending	April 2011–March 2014	–61.0	+24.4
		Descending	August 2011–February 2014	–39.2	+18.6
	Sentinel-1	Ascending	January 2018–December 2022	–41.5	+10.9
		Descending	January 2018–December 2022	–32.7	+12.7
Bologna	ERS-1/2	Ascending	October 1995–September 2000	–49.1	+4.3
		Descending	April 1992–December 2000	–55.4	+10.3
	ENVISAT	Ascending	August 2004–July 2010	–24.0	+5.7
		Descending	November 2003–December 2010	–29.0	+4.8
	Sentinel-1	Ascending	January 2018–December 2022	–25.5	+1.4
		Descending	January 2018–December 2022	–24.1	+8.0
Florence	ERS-1/2	Descending	April 1992–November 2001	–29.5	+11.3
	ENVISAT	Ascending	October 2003–May 2010	–9.3	+6.1
		Descending	February 2003–June 2010	–13.4	+5.2
	Sentinel-1	Ascending	January 2018–December 2022	–13.0	+10.0
		Descending	January 2018–December 2022	–55.6	+0.6

4. Methods

To facilitate a comprehensive spatial analysis and integration of ground deformation stored within the points from each PSInSAR dataset, a uniform grid with ~50 m spacing was generated to cover the administrative boundaries of Rome, Bologna, and Florence, encompassing 693,635, 80,118, and 57,394 grid units, respectively. Attributes derived from each PSInSAR dataset were systematically imported into the grid cells by utilizing the nearest-neighbor interpolation method. Key attributes that were imported included the number of PS within each grid cell, their annual line-of-sight (LOS) displacement velocity, and the corresponding LOS directional cosines. Three scenarios were accounted for, as follows: grid cells containing PS exclusively from ascending orbit data, exclusively from descending orbit data, or a combination of both. To incorporate the maximum amount of information in the following analysis, these three possibilities were all retained in the grid and analyzed accordingly (see Section 4.1), as implemented in [17].

4.1. Estimation of Vertical Displacement Velocity

To accurately represent terrain displacement, it was essential to first convert the LOS velocity estimates into vertical displacement. This was achieved by applying a mathematical approach, as outlined by [17], for each dataset at each grid element.

In instances where data from only a single orbit type, either ascending or descending, were available, the vertical deformation velocity (V_U) was calculated by dividing the LOS velocity (V_{LOS}) by the LOS directional cosine in the vertical direction (U_{LOS}), under the assumption of no horizontal deformation:

$$V_U = V_{LOS} / U_{LOS} \quad (1)$$

when information from both orbits (A, ascending; and D, descending) was available, V_U was computed by considering the east–west (E), north–south (N) and vertical (U) directional cosines of the LOS, and by resolving the following system of two equations:

$$V_A = E_A \times V_E + N_A \times V_N + U_A \times V_U \quad (2)$$

$$V_D = E_D \times V_E + N_D \times V_N + U_D \times V_U \quad (3)$$

In order to resolve the system, the assumption that the N–S displacement is zero was made, following the approach described by [28], and the two unknown variables, V_U and V_E, at each grid cell were derived.

Consequently, this approach allowed for the full potential of the available PS datasets to be effectively harnessed, taking into account the variations in spatial distribution and point density across the datasets, and spatially complementing their information using the regular grid.

To assess the reliability of this method, a comparative analysis of the vertical velocity values derived from each individual orbit type, as well as from the combination of both orbits, was conducted. This comparison is illustrated in Figure 2, where the x-axis represents the ascending mode, and the y-axis represents the descending mode for each study area using the Sentinel-1 datasets. The coefficients of determination (R^2) were 0.91 for Rome, 0.93 for Bologna, and 0.84 for Florence, indicating that the two viewing geometries yield comparable vertical velocity results when used separately or in combination, and further suggesting that horizontal deformation components are negligible across large proportions of the three study areas, as most observations align closely with the 1:1 regression line.

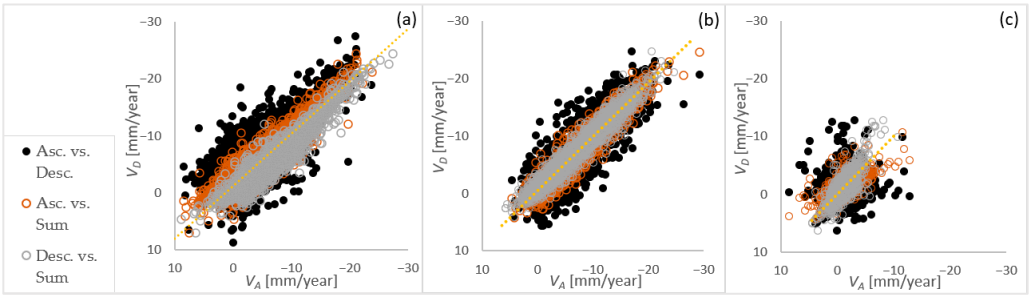

Figure 2. Comparison of the vertical displacement velocity derived using the Sentinel-1 datasets, for (**a**) Rome, (**b**) Bologna, and (**c**) Florence. The linear regression between ascending and descending mode geometries is represented with a dashed yellow line. Notation: 'Asc.', ascending; 'Desc.', descending; 'Sum', combined ascending and descending.

4.2. Angular Distortions and Hazard Assessment

The assessment of subsidence-induced hazards extends beyond the evaluation of V_U or the total settlement (d_U), as it incorporates the differential settlement (Δd_U) occurring between two points relative to their distance (l), which in turn results in angular distortion (β) during a given period (t) [16,17]:

$$\beta_t = \Delta d_U / l \quad (4)$$

β is a critical parameter widely employed in geotechnical engineering to evaluate the potential severity of damage, such as the development of cracks, fractures, tilts, and other forms of structural impairment caused by the strain imposed on urban infrastructure due to differential settlement [29,30].

To calculate β for the three cities, V_U derived from each PSInSAR dataset were multiplied by the total duration of the observed period, thereby yielding d_U for each time interval, at each grid element. The longest period between the ascending and descending orbit pairs of the same satellite was utilized, under the assumption of temporal correspondence between ascending and descending datasets, and the occurrence of steady deformation rates during the monitoring periods. For example, for Rome, this temporal duration spans 8.2 years for ERS-1/2 datasets, 7.6 years for ENVISAT, 2.7 years for COSMO-SkyMed, and 5 years for Sentinel-1. The distance l is equal to 50 m, as it corresponds with the grid resolution employed to resample the datasets.

Furthermore, to compute the total angular distortion (β_T) accumulated over the 30-year period analyzed, from 1992 to 2022, some additional assumptions were necessary. Notably, there are temporal gaps between the different datasets employed: 3 years between ERS-1/2 and ENVISAT, 8 years between ENVISAT and Sentinel-1 for Bologna and Florence, and for Rome, 1 year between ENVISAT and COSMO-SkyMed, and 3.6 years between COSMO-SkyMed and Sentinel-1. To derive an estimate of d_U occurred during the entire three-decade period, the V_U during these temporal gaps was assumed to be constant and equal to the average of the velocities from the preceding and succeeding datasets. The β_T values were then calculated only for the grid elements where the three (or four) datasets were all present.

To assess the potential impact of differential subsidence to urban infrastructure, following [9,16,17] and accounting for both geotechnical practice [29] and existing InSAR-based subsidence studies [31,32], the hazard was classified into four categories, based on the β accumulated over the 30 years: low ($\beta_T < 0.03\%$), medium ($0.03\% \leq \beta_T < 0.06\%$), high ($0.06\% \leq \beta_T < 0.2\%$), and very high ($\beta_T \geq 0.2\%$), indicative of increasing hazard severity. When assessing hazards for a subset monitoring period, the three thresholds (0.03%, 0.06%, and 0.2%) were adapted proportionally to the duration of the selected period with respect to the 30 years (e.g., for the Sentinel-1 period, they were adjusted using the 1/6 proportion into 0.005%, 0.01%, and 0.033%, respectively).

4.3. Infrastructure Exposure–Vulnerability Analysis

In order to assess exposure (i.e., location, attributes, and value of assets) and vulnerability (i.e., the likelihood that assets will be damaged/destroyed/affected when exposed to subsidence-induced hazards) of the elements at risk (i.e., urban infrastructure), land use/cover information and population data obtained from the UA dataset were exploited.

Each UA polygon was scored according to the type and attributes of the infrastructure involved, assigning scores from 1 to 4 based on an increased level of exposure and vulnerability (1: low; 2: medium; 3: high; 4: very high), as shown in Table 1. The highest score was assigned to continuous and discontinuous dense urban fabric with the sealing level (S.L.) exceeding 80% and between 50 and 80%, respectively (UA codes 11100 and 11210): strategic transport infrastructure including airports, railways, and fast transit roads (UA codes 12400, 12210 and 12230). Moving toward less dense urban fabric, industrial sites, minor roads, and vegetated lands, lower scores were assigned, from 3 to 1. The category "not applicable" (NA) was used for water bodies and wetlands.

4.4. Subsidence-Induced Risk Assessment

A risk matrix was developed, combining the subsidence-induced hazard levels derived from the satellite PSInSAR datasets, with the type of infrastructure exposed as mapped in the UA and the associated exposure–vulnerability scores. Considering both parameters, it was possible to identify 4 risk categories: low, medium, high, and very high, as shown in Table 3. This approach allowed for a comprehensive evaluation of the risk levels associated with different types of urban infrastructure and also for the quantification of the population residing in them, being able to determine the number of people affected in each UA polygon. For instance, when areas with critical infrastructure types (e.g., bridges, dense urban fabric; scored 4 for exposure–vulnerability), which typically have high population density, exhibit significant angular distortion values (very high hazard) are classified as at very high risk. On the other hand, green spaces (which typically do not involve residents) yield low risk when affected by up to a medium hazard.

Table 3. Proposed subsidence-induced risk matrix combining hazard levels based on angular distortion (β), with exposure–vulnerability based on UA land use/cover type. Possible hazard levels are: low (green), medium (yellow), high (red) or very high (dark-red).

		Hazard (β Categories)			
		Low	**Medium**	**High**	**Very High**
Exposure–Vulnerability	**Low**	Low	Low	Medium	Medium
	Medium	Low	Medium	Medium	High
	High	Medium	Medium	High	High
	Very High	Medium	High	High	Very High

5. Results

5.1. Multi-Decadal Land Subsidence Evolution

The application of multi-temporal and multi-sensor PSInSAR analysis yielded detailed ground deformation velocity maps, revealing subsidence evolution in both spatial and temporal dimensions over the last thirty years. The 50 m resolution vertical displacement velocity (V_U) maps obtained by combining ascending and descending mode datasets (see Section 4.1) are shown in Figure 3, corresponding to the latest period analyzed for the cities of Rome (Figure 3a), Bologna (Figure 3b), and Florence (Figure 3c) (while the maps of the different temporal periods area provided in Figures A1–A3 in Appendix A). Negative V_U values indicate land subsidence, while positive values indicate uplift. A range of –3 to +3 mm/year was considered to identify stable values (displayed as green areas in Figure 3). It is worth noting that spatial gaps in the coverage of the deformation products across the study areas indicate zones not covered by the PSInSAR results, due to the lack of PS (e.g., attributable to temporal decorrelation over rural lands, not allowing the identification of good radar reflectors across the image stacks).

Three specific areas were selected for each city to evaluate their temporal behavior in detail, one considered stable (RM.1, FI.1, BO.1) and two considered hotspots of ground displacement (RM.2, RM.3, FI.2, FI.3, BO.2, BO.3); though, it is important to note that this same analysis could be replicated in detail for each processed pixel.

For both Rome and Florence, the V_U maps generally show stable values, with the exception of some affected sectors. In Rome, there are lower V_U values along the margins of the Tiber River (RM.2) and the southwestern area, along the corridor to Fiumicino (RM.3). In Florence, the lower V_U values are located at the northwestern area of the city (FI.2) and on the Trespiano cemetery (FI.3). On the other hand, in Bologna, a very big, affected area is observable for the first two periods of analysis (from 1992 to 2010) spanning from the center to the northern part of the city, while decreasing V_U values are found for the last period analyzed (2018 to 2022). The two selected areas correspond with the historical city center (BO.2) and the northeastern part of the city (BO.3).

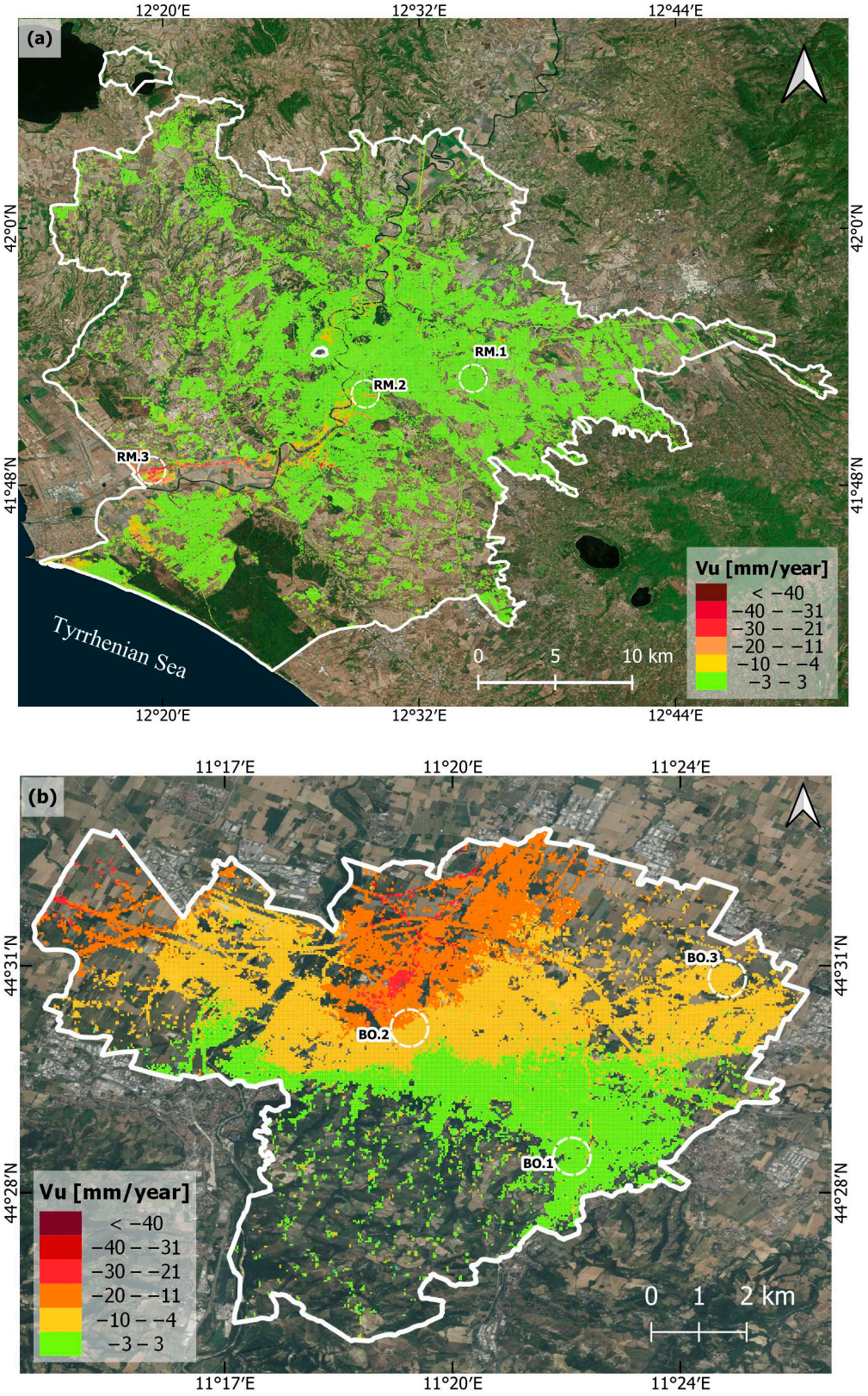

Figure 3. *Cont.*

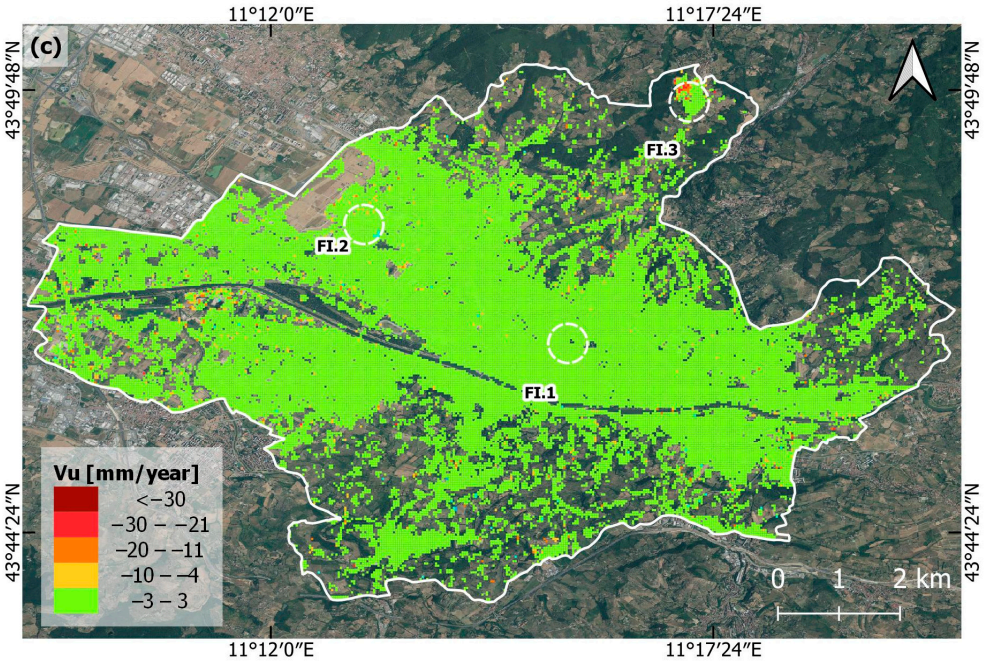

Figure 3. Vertical displacement velocity (V_U) maps of the 2018–2022 period for the city of Rome (**a**), Bologna (**b**), and Florence (**c**). PSInSAR data are overlapped onto Google Earth imagery.

For a more detailed analysis of land subsidence trends in the 1992–2022 period, the d_U and V_U values of the three sample locations selected within each study area were analyzed (Figure 4). A variability of the d_U behavior between the three studied cities can be observed. The time series for Rome show generally stable d_U for RM.1, indicating minimal natural movements in this area. In contrast, RM.2 and RM.3 exhibit significant d_U, with values reaching approximately –280 mm over the observation period, also revealing fluctuating yearly V_U (calculated for each single year via the linear regression of the respective d_U subset values), with negative peaks in the first three periods, between 1992 and 2014, and more stable yearly V_U in 2018–2022. On the other hand, Bologna's d_U time series show significant subsidence in BO.2 and BO.3, with d_U exceeding –600 mm, while B.1 remains relatively stable with minimal d_U. The most severe yearly V_U trends for BO.2 and BO.3 are evident in the early observation period. The yearly V_U appears to fluctuate significantly before 2010, with a slight reduction only after 2010. The difference with this city is that for the first period a correlation between the yearly V_U peaks is observed, which could be a sign of a more generalized pattern. In the case of Florence, the highest d_U (absolute value) is observed in FI.2, reaching up to –430 mm, but both FI.2 and FI.3 show persistent negative yearly V_U, indicating ongoing subsidence. The yearly V_U is more pronounced during the first and last periods, with a slight stabilization observed in 2003–2010.

5.2. Differential Subsidence Hazard

To assess the potential impact of differential subsidence to urban infrastructure in the three cities, angular distortion maps were generated for Rome (Figure 5), Bologna (Figure 6), and Florence (Figure 7), also detailing the hotspots with the highest V_U that were analyzed in the previous section, and that were then exploited to classify subsidence-induced hazards in four classes, from low to very high (see Section 4.2).

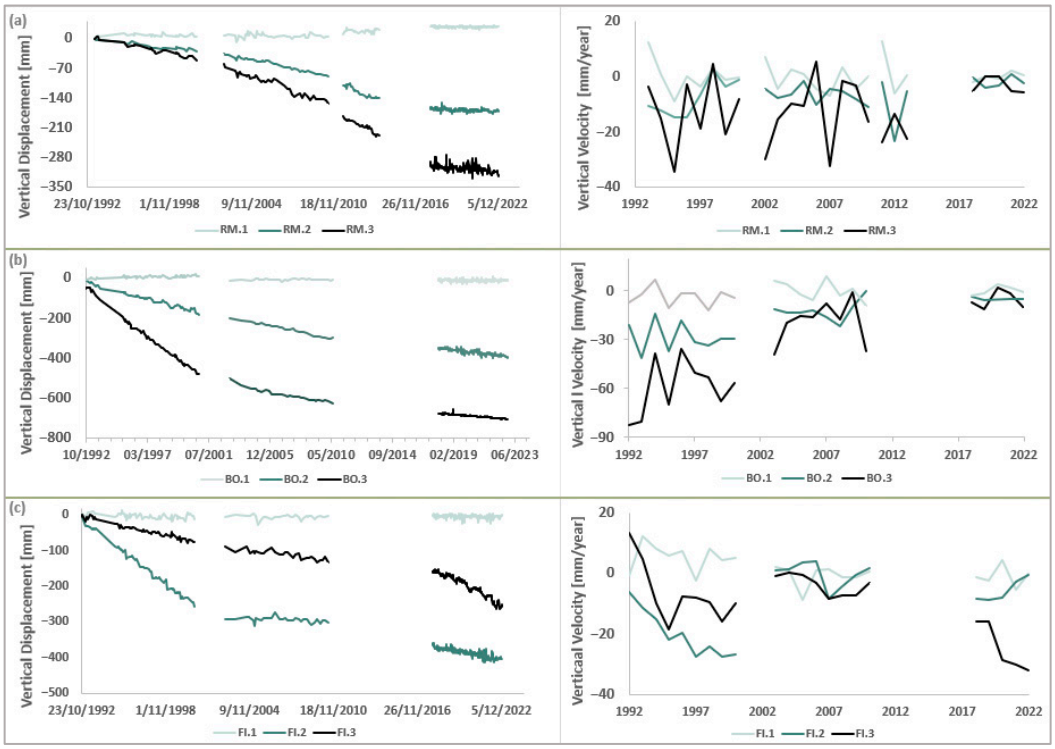

Figure 4. Vertical displacement (d_U) and yearly vertical displacement velocities (V_U) time series corresponding to the sample locations selected for (**a**) Rome, (**b**) Bologna, and (**c**) Florence.

In the case of Rome, the highest β_T are observed along the margins of the alluvium of the Tiber River and its tributaries. Various types of infrastructure, including buildings, streets, and bridges that cross the river are affected (zoom II in Figure 5a,b), reaching up to 0.2% β_T, which represents a differential settlement of 0.15 m across a 50 m distance, generated during the 30-year period analyzed. Another significantly affected area is located to the southwest of Rome city center, in the direction of Fiumicino, where the Leonardo Da Vinci International Airport is located (zoom I), observing the primary impact on the highway that connects the metropolitan city with the airport, with peaks of 0.33% β_T, which means 0.165 m of the total differential settlement across 50 m during the 30 years of observation. The land affected by very high and high hazard, by looking at the whole period of 30 years, extends 31.89 km^2 and 5.01 km^2, respectively (Table 4).

For Bologna, the higher hazard values are observed in the first period of analysis, before 2000, spanning from the northern sector of the city center to the administrative area's northern boundary, where industrial expansion has taken place (Figure 6a,b). In this sector, $\beta_{1992–2000}$ reaches values as high as 0.13%, indicating the differential settlements of 0.065 m across a 50 m distance (Figure A5 in Appendix A). The pronounced pattern with high angular distortion values in the center of the study area would highlight the sharp difference between areas affected by subsidence (to the north) and those unaffected (to the south), resulting in a higher differential settlement, hence angular distortion. No very-high-hazard zones were found in 1992–2000 (Table 4), i.e., no $\beta_{1992–2000}$ values exceeding 0.2%, which is the typical threshold used to identify a high probability of severe damage to urban infrastructure [18,29]. However, the subsequent periods reveal decreasing and more focused hazard zones (Figure A5 in Appendix A, and Figure 6b), indicating an overall decrease in land subsidence hazard levels across the city (Table 4), e.g., from 0.62 km^2 of high hazard and 11.41 km^2 of medium hazard in the 1990s, to no high hazard and 0.24 km^2 medium hazard in 2018–2022. Furthermore, as a result of the high resolution of the conducted analysis, it is possible to identify the specific urban infrastructures affected. Examples include the main city center (zoom I), and a sector at the northeast of the study area (zoom II), which includes some urban infrastructure, such as the Provincial Office of

Civil Motorization, a railway test circuit, a residential area, and the Italian Food Theme Park (FICO).

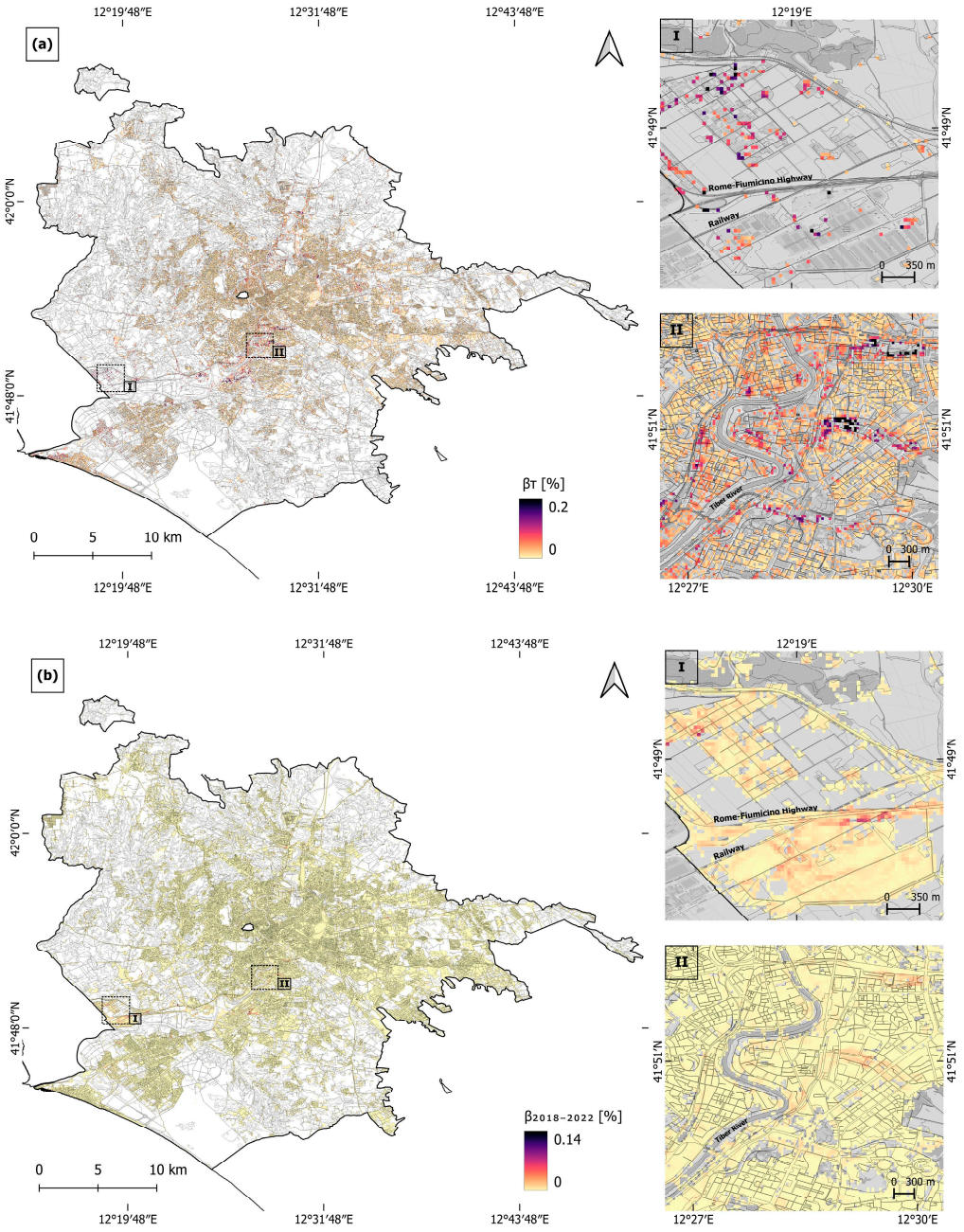

Figure 5. Rome hazard maps, representing (**a**) the 30-year period angular distortion, β_T, and (**b**) the 2018–2022 period angular distortion, $\beta_{2018–2022}$. The 2018 Urban Atlas layer is superimposed and zooms (I) and (II) are overlapped onto the OpenStreetMap on grey scale.

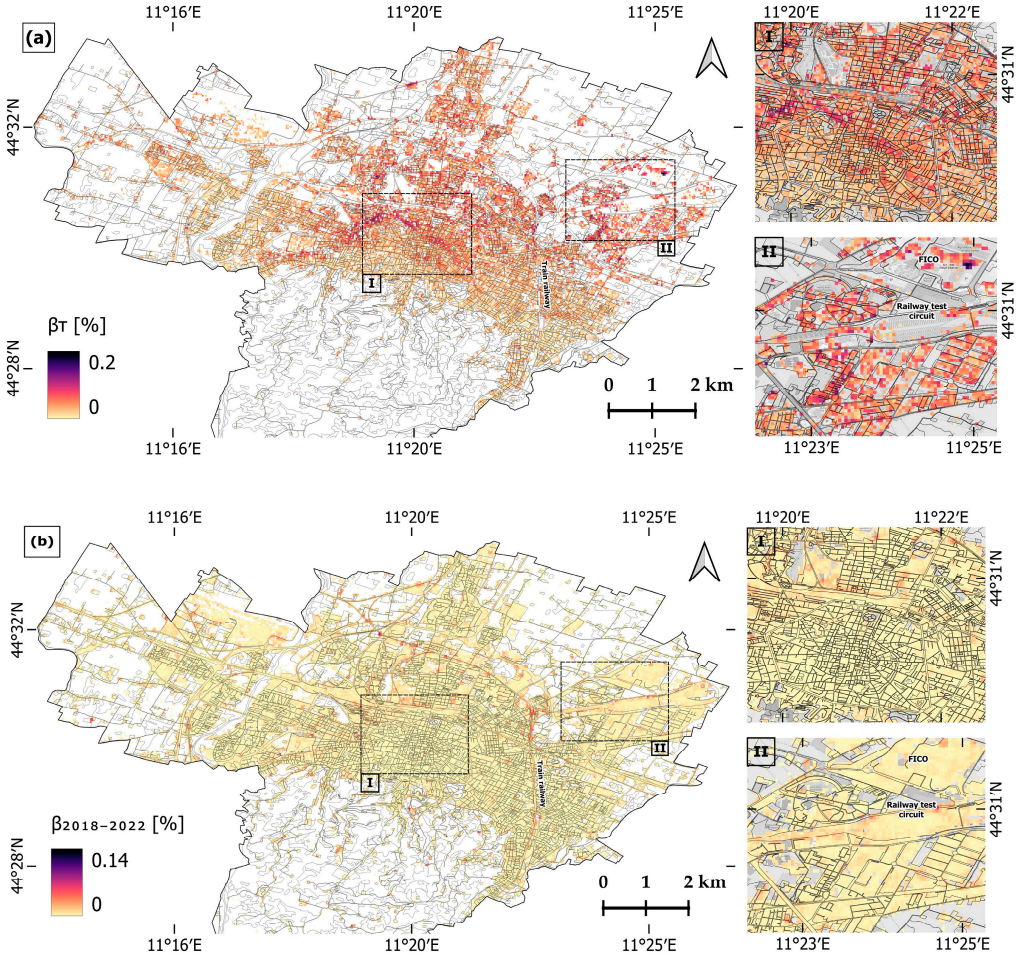

Figure 6. Bologna hazard maps, representing (**a**) the 30-year period angular distortion, β_T, and (**b**) the 2018–2022 period angular distortion, $\beta_{2018–2022}$. The 2018 Urban Atlas layer is superimposed and zooms (I) and (II) are overlapped onto the OpenStreetMap on grey scale.

It is noteworthy that owing to the substantial volume of PS data in the Sentinel-1 datasets, a highly detailed angular distortion map was obtained (Figure 6b), where medium- and high-hazard zones can be identified clearly along the train railway. In this case, $\beta_{2018–2022}$ is between 0.012% and 0.05% along the ~11.4 km railway line, indicating differential settlements of up to 0.006 m and 0.025 m, respectively, across 50 m distances. Regarding β_T (Figure 6a), the highest values are located in the northwestern half of the city center, following the previously described pattern, reaching up to 0.2% β_T, which corresponds to the total differential settlements of 0.1 m across 50 m during the 30 years of observation. These high values extend toward the northern part of the administrative area, with the highest β_T at the northeastern sector analyzed, where infrastructure such as a railway test circuit and shopping centers are located.

On the other hand, Florence shows a general ground stability, with low hazard values for most of the city (Figure 7a,b and Table 4), except for a few hotspots of differential settlement consistent over time, as seen in the northwest sector (zoom I), at the cemetery (zoom II), and some in the margins of the Arno River. β_T in the northwestern sector reaches up to 0.17% and at the cemetery up to 0.08%, corresponding to the differential settlements of 0.085 m and 0.04 m, respectively, classifying both as high-hazard zones, showing an increment of the β during the last period analyzed.

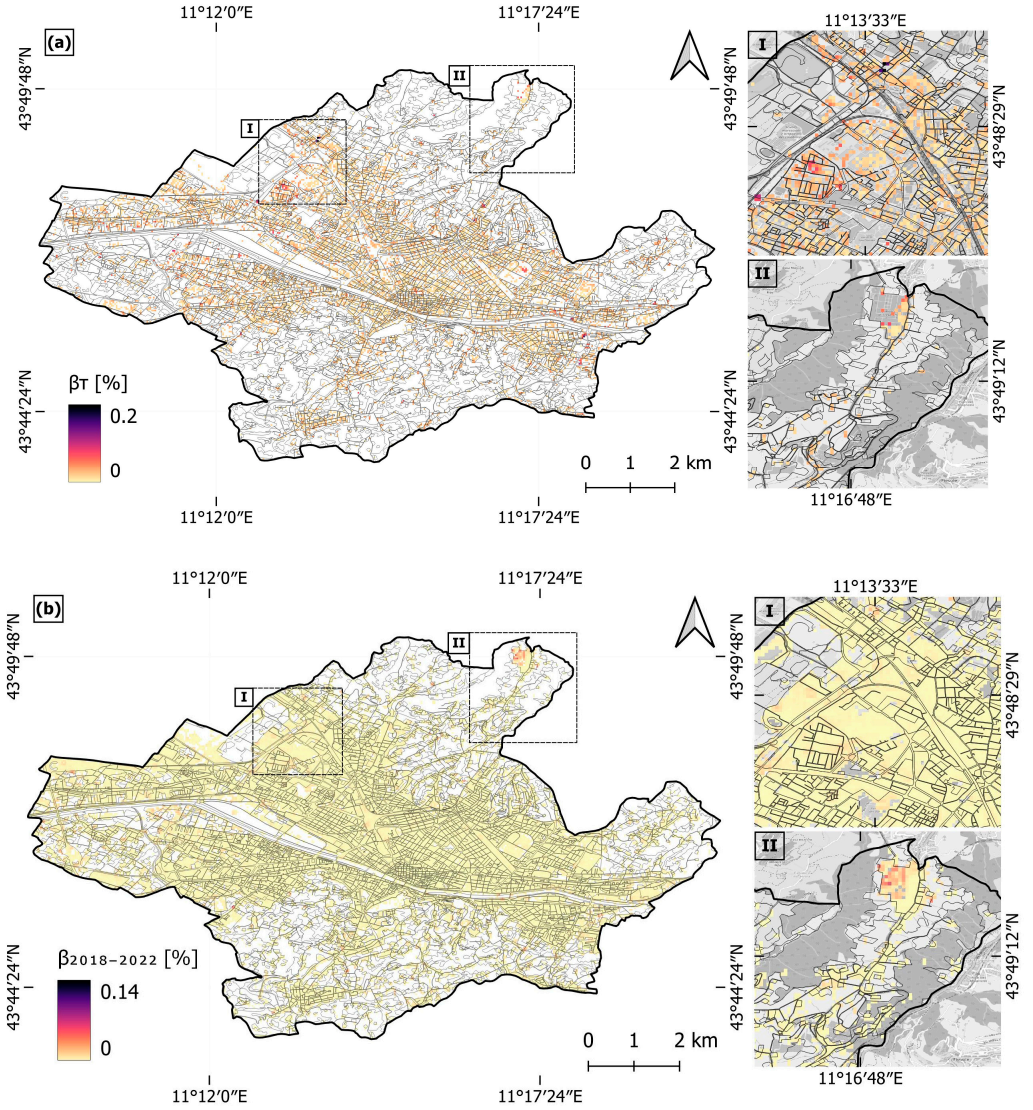

Figure 7. Florence hazard maps, representing (**a**) the 30-year period angular distortion, β_T, and (**b**) the 2018–2022 period angular distortion, $\beta_{2018–2022}$. The 2018 Urban Atlas layer is superimposed and zooms (I) and (II) are overlapped onto the OpenStreetMap on grey scale.

Table 4. Extent of subsidence-induced hazard classes within the three cities, over the 30-year monitoring period. Notation: ND, no data.

Study Area	Period	Low [km^2]	Medium [km^2]	High [km^2]	Very High [km^2]	ND [km^2]
Rome	1992–2000	226.49	1.84	0.04	0	1058.88
	2002–2010	306.70	2.20	0.01	0	978.33
	2011–2014	530.26	3.49	0.01	0	753.48
	2018–2022	527.95	2.35	0.01	0	756.94
	1992–2022	142.34	31.89	5.01	0.14	1107.86
Bologna	1992–2000	54.55	11.41	0.62	0	74.29
	2003–2010	43.43	0.24	0	0	97.18
	2018–2022	76.35	0.23	0	0	64.38
	1992–2022	16.29	15.88	4.82	0	103.85

Table 4. *Cont.*

Study Area	Period	Low [km^2]	Medium [km^2]	High [km^2]	Very High [km^2]	ND [km^2]
Florence	1992–2001	27.52	0.06	0.02	0	74.72
	2003–2010	44.65	0.06	0	0	57.62
	2018–2022	66.20	0.14	0	0	35.97
	1992–2022	19.07	1.98	0.14	0.01	81.12

5.3. Risk Mapping and Affected Population

Implementation of the exposure–vulnerability scoring to the UA dataset (see Section 4.3) provided an overview of the spatial distribution of the elements at risk that could be mostly damaged and generate the greatest loss, if exposed to subsidence-induced hazards (Table 5 and Figure 8). In Rome, the very high exposure–vulnerability land amounts to 135.53 km^2, whilst the area classified at high exposure–vulnerability extends 259.76 km^2 (Figure 8a). In Bologna, the same two classes extend 15.91 and 51.68 km^2, respectively (Figure 8b), while in Florence they cover 15.61 and 37.32 km^2, respectively (Figure 8c).

Table 5. Extent of exposure–vulnerability classes within the three cities. Notation: NA, not applicable.

Study Area	Low [km^2]	Medium [km^2]	High [km^2]	Very High [km^2]	NA [km^2]
Rome	762.55	59.70	259.76	135.53	69.71
Bologna	65.37	6.74	51.68	15.91	1.15
Florence	41.58	6.12	37.32	15.61	1.68

By applying the risk matrix methodology (see Section 4.4), risk maps for the three cities were generated for both the total distortion over the 30 years (β_T, referred to 1992–2022) and the most recent period analyzed ($\beta_{2018–2022}$), the latter allowing for greater spatial coverage thanks to the Sentinel-1 EGMS datasets and also providing the most updated subsidence-induced risk scenario (Figures 9–11).

The risk assessment results for Rome, Bologna, and Florence provide a detailed breakdown of the areas and populations affected by the total differential subsidence which occurred during the 30-year period (Figure 12). The values within each bar represent the absolute area (in square kilometers) and population (in thousands) corresponding to each risk category. The three cities exhibit significant medium-risk areas, encompassing 597.6 km^2 for Rome affecting 2,454,430 inhabitants, while for both Bologna and Florence it corresponds to ~44 km^2, affecting 215,393 (85%) and 349,016 (90%) inhabitants, respectively. This highlights the need for targeted monitoring efforts in these relatively large zones. In terms of very high risk, Rome is the only city where this category was found, involving 0.14 km^2 that includes 994 inhabitants. While for the high-risk category, Rome and Bologna show the highest percentages: Rome has 36.01 km^2 with 164,617 inhabitants in the high-risk category, whereas Bologna has 11.44 km^2 with 130,663 inhabitants. In such zones, especially in the very high-risk ones, tailored field checks and monitoring would be needed to verify the conditions of the urban infrastructure and the potential development of any fractures/cracks or other types of structural damage in the buildings and transport networks.

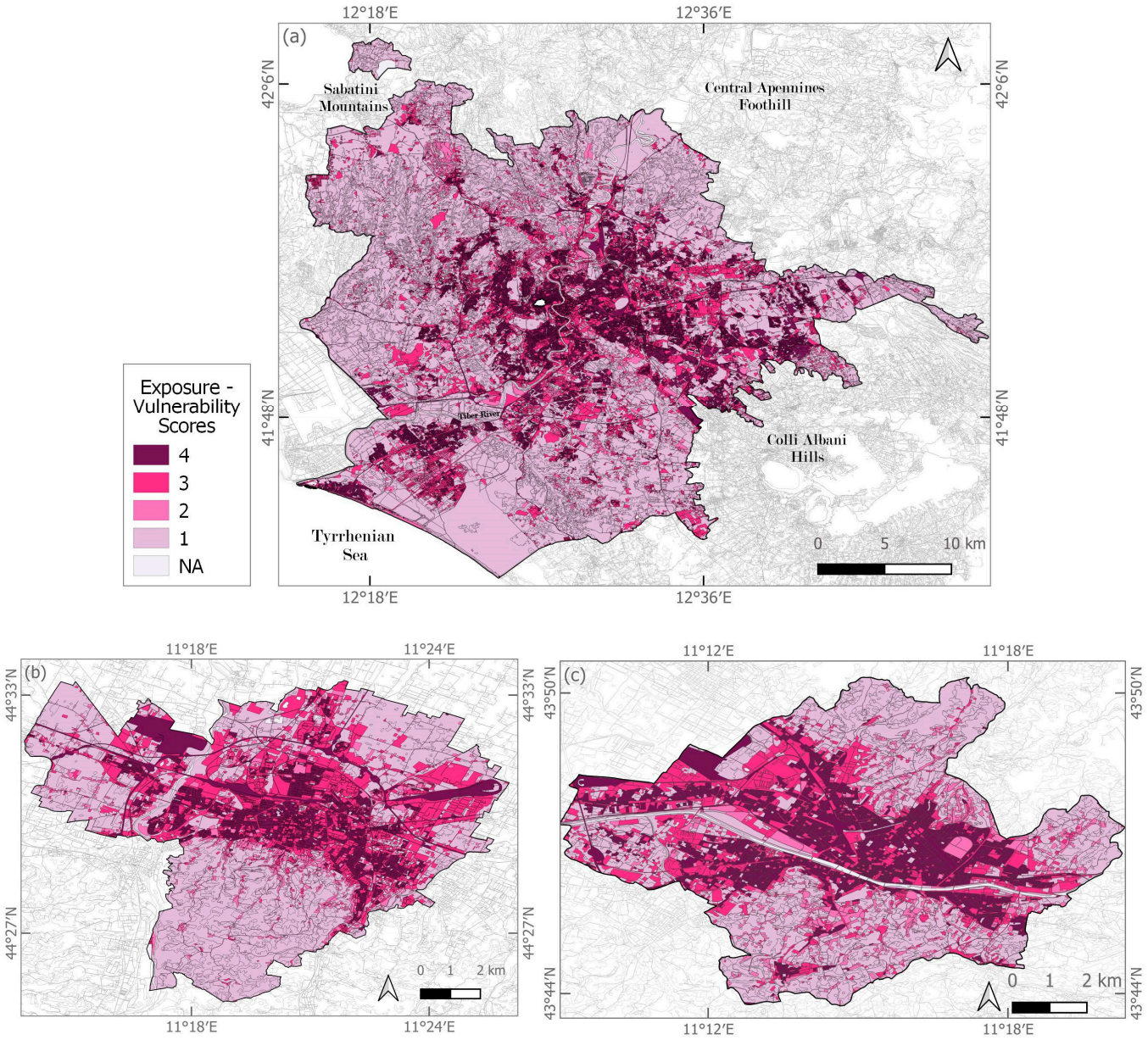

Figure 8. Exposure–vulnerability of urban infrastructure in (**a**) Rome, (**b**) Bologna, and (**c**) Florence, based on scoring of UA 2018 classes.

It is noteworthy that despite Florence generally exhibiting low values of vertical displacement velocity, these have been continuous over time. This persistent subsidence has accumulated moderate angular distortion over the years, resulting in a high percentage of areas potentially exposed to medium risk (Figure 11). This demonstrates that even low-velocity subsidence, if sustained, can significantly impact urban infrastructure by allowing differential settlement to gradually develop over time.

On the other hand, it is important to highlight that, despite the high percentages of "no data" (where no hazard information was available, due to lack of PSInSAR data coverage), this is affecting only low percentages of the population, as the lack of hazard information mostly occurs across land covers that are typically not hosting a population, e.g., green urban areas, vegetated lands.

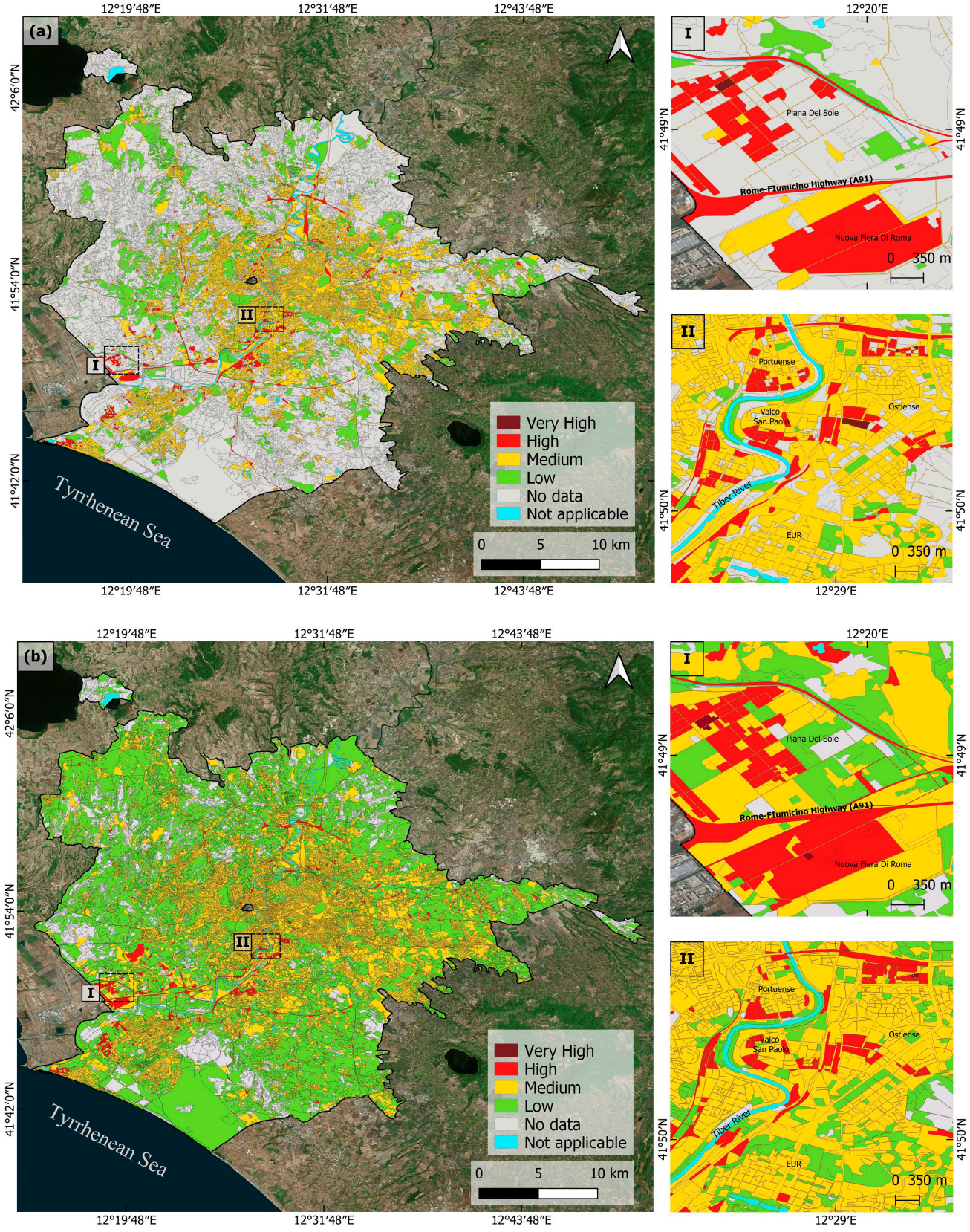

Figure 9. Subsidence-induced risk in Rome, assessed by exploiting the risk matrix combining angular distortion and exposure–vulnerability scores: risk mapping referred to (**a**) the 30-year period 1992–2022, and (**b**) the 2018–2022 period. Risk maps are overlapped onto Google Earth imagery.

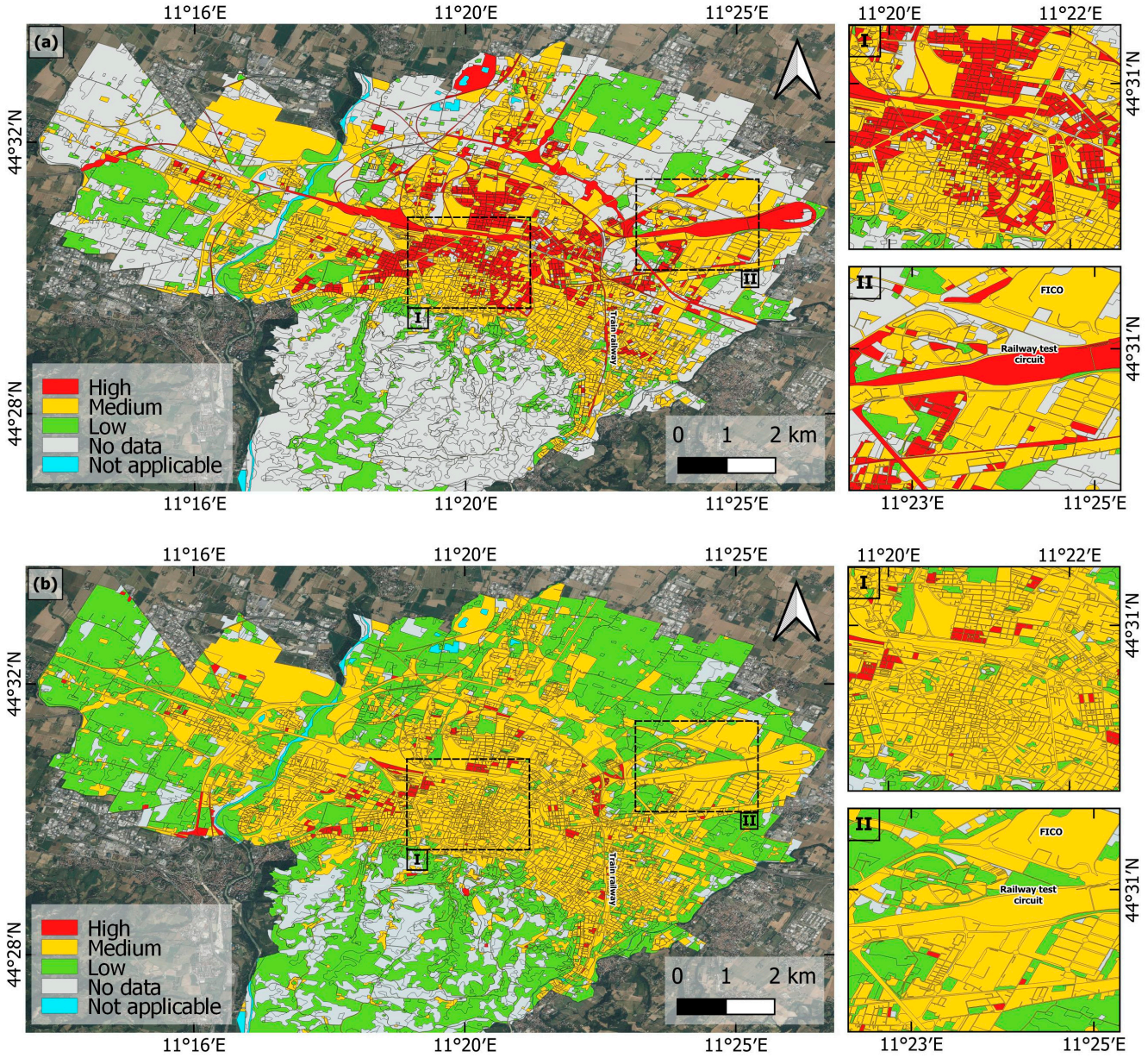

Figure 10. Subsidence-induced risk in Bologna, assessed by exploiting the risk matrix combining angular distortion and exposure–vulnerability scores: risk mapping referred to (**a**) the 30-year period 1992–2022, and (**b**) the 2018–2022 period. Risk maps are overlapped onto Google Earth imagery.

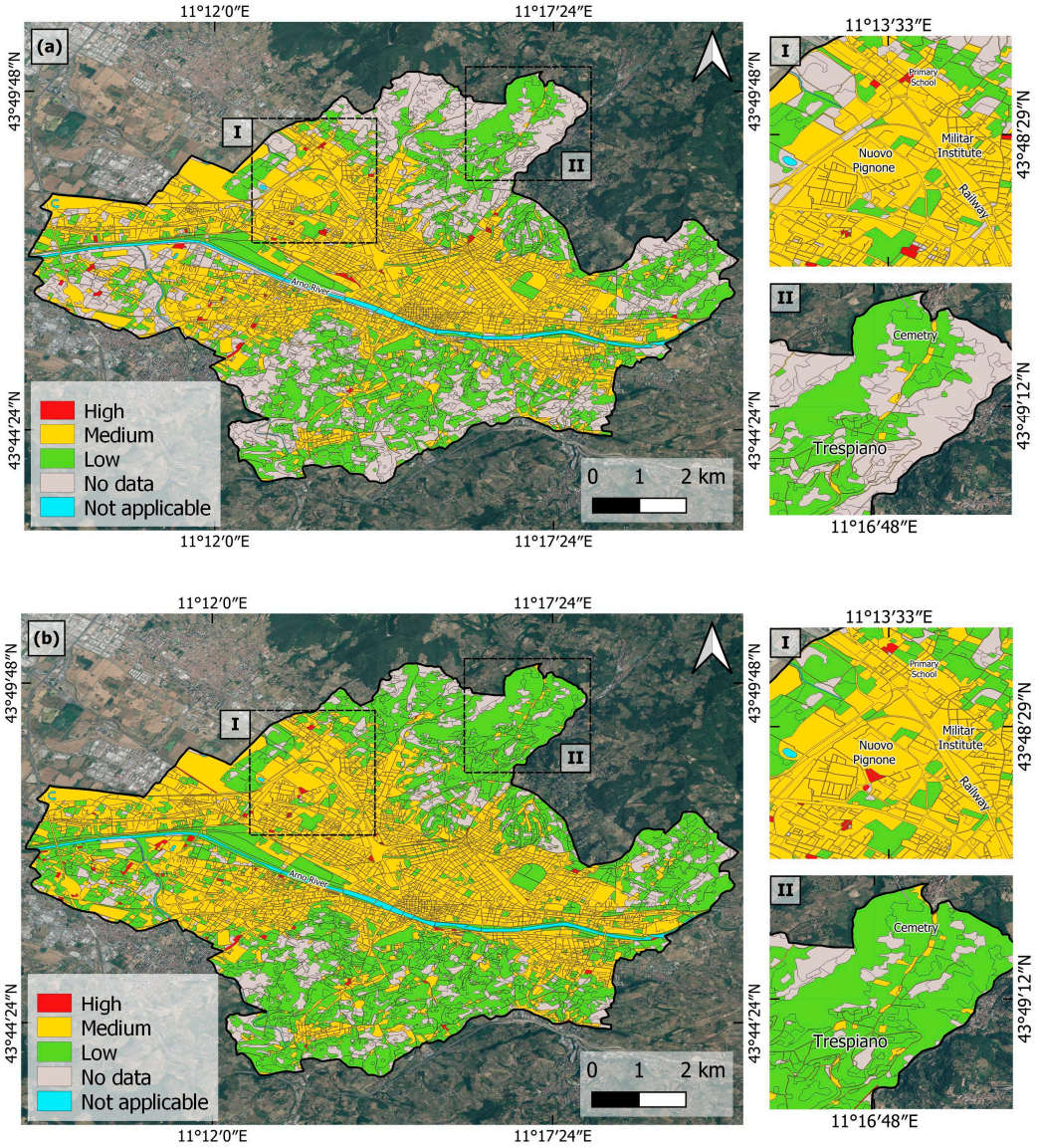

Figure 11. Subsidence-induced risk in Florence, assessed by exploiting the risk matrix combining angular distortion and exposure–vulnerability scores: risk mapping referred to (**a**) the 30-year period 1992–2022, and (**b**) the 2018–2022 period. Risk maps are overlapped onto Google Earth imagery.

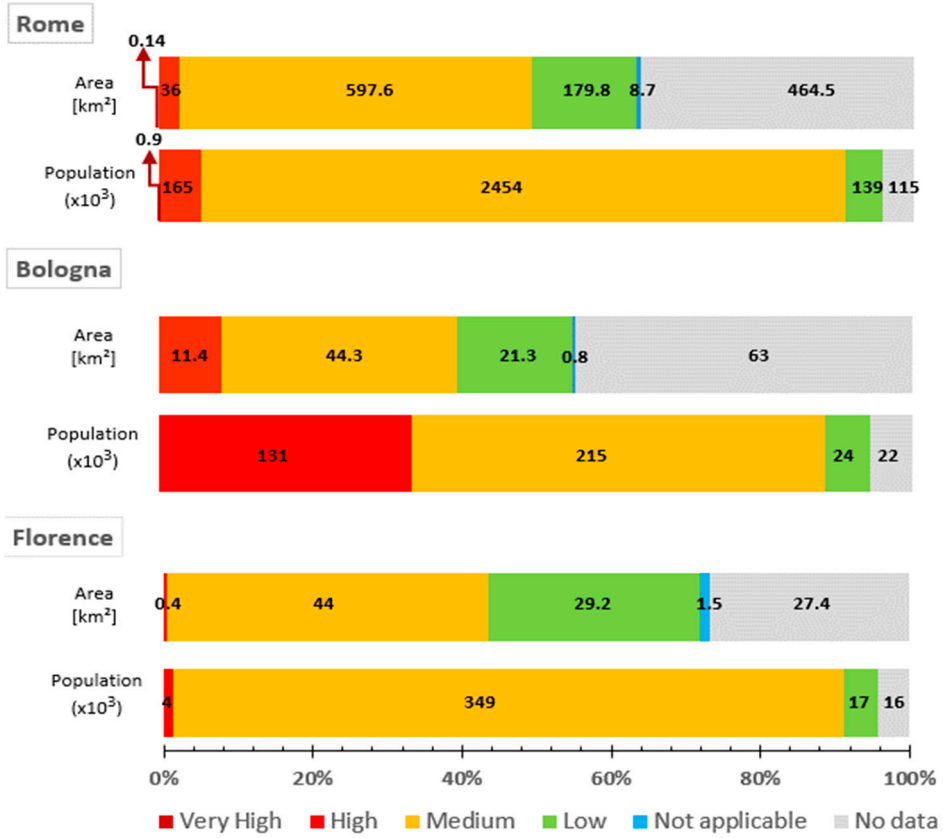

Figure 12. Overview of the subsidence-induced risk mapping statistics for Rome, Bologna, and Florence in 1992–2022, highlighting the amount of square kilometers of land and population involved in each risk category. Note that each bar represents 100% of the area of each city.

6. Discussion

The implemented risk assessment methodology involved the generation of a risk matrix combining subsidence-induced hazards with geospatial data from the Copernicus Urban Atlas, which enabled the creation of detailed risk maps based on the type and attributes of affected urban infrastructure. The thresholds established for categorizing hazard levels align with those utilized in prior risk assessment studies conducted in other countries, such as Mexico [9,16,17], Nigeria [18], Brazil [32], and the United States [33]. Notably, this study represents the first instance of applying this methodology and thresholds comprehensively across three cities in Italy. Moreover, it is the first time that InSAR-derived hazard assessment has been combined with the Copernicus Urban Atlas data, enabling the evaluation of vulnerability and exposure factors for a more accurate risk assessment at the urban block level.

The findings of this study on the highest subsidence-induced risk areas in Rome, Bologna, and Florence are consistent with the previously published literature, which has identified these zones as critical. For instance, in Rome, the results indicate that the area of the highway to Fiumicino (RM.3) and the margins of the Tiber River alluvium, especially along Via Giustiniano Imperatore (RM.2), are very-high-risk zones, corroborating earlier research that had highlighted this region's vulnerability to subsidence (e.g., [34] and [35], respectively). This last case is shown in Figure 13, where it is possible to observe the correlation between the change in the type of lithology and the differential subsidence patterns (and higher values of the 30-year angular distortion) along the edge of the alluvial fan deposits (Figure 13b), areas which are then classified as very high to high risk (Figure 13c). Similarly, in Florence, several of the red polygons in the generated risk maps align with areas identified as critical in other studies, such as [36]. Furthermore, the subsidence pattern evolution observed over time and space in Bologna aligns with findings from

previous geohazard investigations (e.g., [23,37]). Specifically, the most affected area spans from the historical city center toward the north, a zone predominantly classified as high risk in this study. These consistencies reinforce the validity of the present risk assessment methodology and highlight the critical areas that require focused monitoring efforts. For land management purposes, ideally, the 3-decade risk assessment maps (1992–2022) should be exploited to gather a long-term overview of the distribution of risk levels across the cities, while the 2018–2022 maps should be considered for the detailed analysis of the most recent risk scenario.

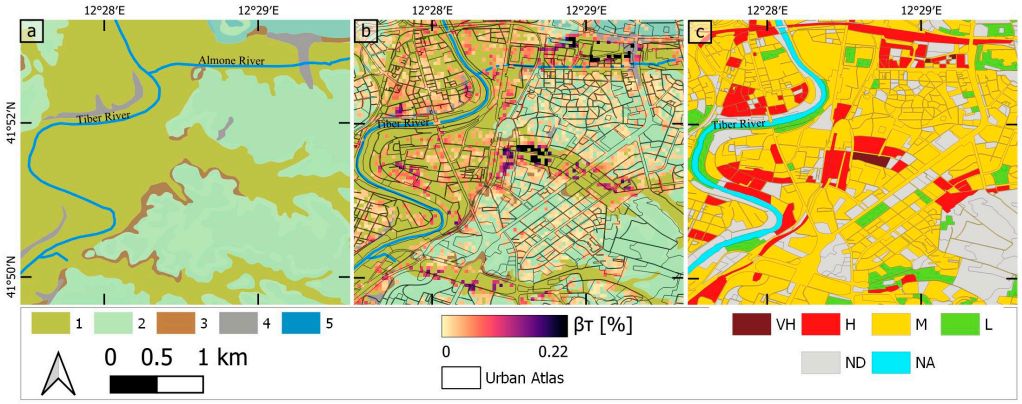

Figure 13. Example of correlation between lithology, subsidence, and resulting risk in Rome. (**a**) Lithology map representing (1) alluvial fan deposits, (2) pozzolana, (3) marginal sandy facies, (4) anthropogenic deposits, and (5) river, obtained from Lazio Region open data catalog; (**b**) total angular distortion values with Urban Atlas polygons superimposed; and (**c**) risk map for the 1992–2022 period. Notation: VH, very high; H, high; M, medium; L, low; ND, no data; NA, not applicable.

The causes of land subsidence are diverse and extend beyond the scope of this study; however, based on the literature and the analysis conducted, it can be inferred that each of the three cities investigated in this work faces a different primary cause of ground instability, not always limited to land subsidence. In Rome, the predominant factor appears to be the type of lithology, particularly in areas where alluvial fan deposits are prevalent and gradually compact (Figure 13). In Bologna, as demonstrated in previous studies (e.g., [23]), the overexploitation of aquifers for water supply has been identified as the leading cause of the observed subsidence pattern. This is exemplified in Figure 14, which highlights an area with a groundwater monitoring well that registers a negative measurement of −11.45 m. Meanwhile, in Florence, landsliding plays a crucial role in ground instability at the local scale in some sectors of the city, as evidenced by the geohazard mapping databases (Figure 15). As showcased in the final example focusing on the Trespiano cemetery, although the area is affected by high angular distortion due to significant differential settlements, the assessed risk remains low across most of the area, due to its classification as a green urban area, which inherently reduces its vulnerability.

However, several limitations of the proposed risk assessment methodology must be acknowledged. The Urban Atlas Land Cover/Land Use dataset, while providing extensive spatial coverage and building block level data, if used on its own it lacks detailed information on critical building characteristics such as height, construction type, foundation types, and maintenance status. These characteristics are essential for a precise vulnerability assessment to subsidence. The absence of this information may result in inaccuracies in risk estimation, potentially leading to either an underestimation or overestimation of the actual risk in specific areas. Future research could therefore focus on incorporating additional datasets to account for these parameters, for instance, the Urban Atlas Building Heights dataset, which is made available for core urban areas at 10 m spatial resolution for the reference year 2012.

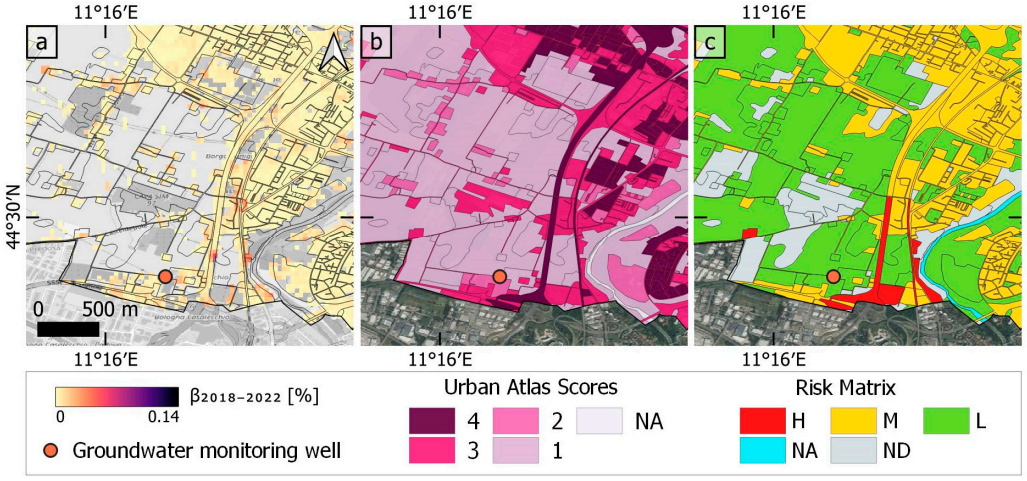

Figure 14. Example of correlation between groundwater extraction, subsidence, and derived risk in Bologna: (**a**) 2018–2022 angular distortion values with Urban Atlas polygons superimposed. The orange dot represents the position of ARPAE'S groundwater monitoring well (modified from [38]). The recorded change in its piezometric level is −11.45 m. (**b**) Exposure–vulnerability of urban infrastructure. (**c**) Risk map for the 2018–2022 period.

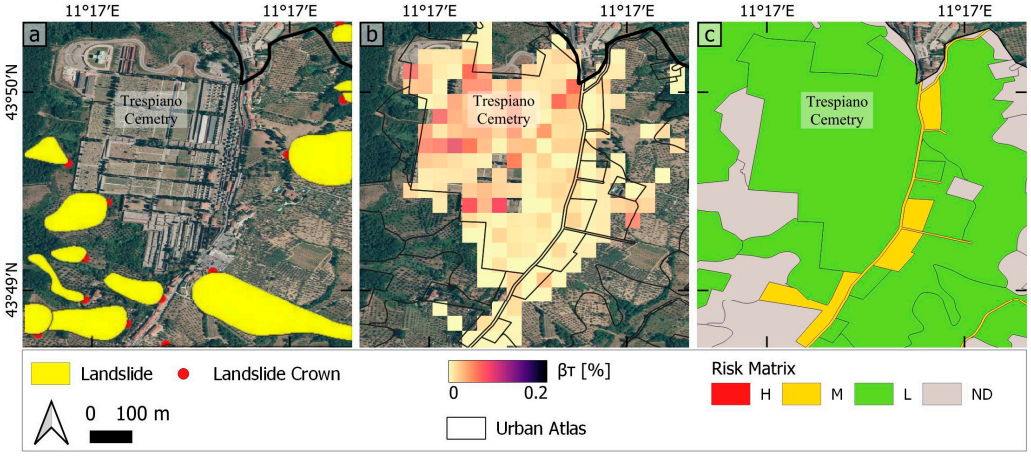

Figure 15. Example of correlation between landslide processes and ground displacement measured in Florence. (**a**) Shows the landslides in the study area, obtained from the Italian Landslide Inventory (IFFI project), (**b**) total angular distortion map, and (**c**) the risk matrix map.

Furthermore, the utilization of a 50 m grid for the data analysis, while offering a broad overview, fails to capture subsidence impacts at the granularity of individual buildings or structures. This can lead to a generalized risk assessment that may overlook specific vulnerabilities within smaller areas. Moreover, the grid resolution might not sufficiently represent the variability of subsidence within larger urban blocks, resulting in the possible misclassification of risk levels. The use of a smaller grid would therefore be recommended for local-scale risk assessments, though this would have to be traded off with the spatial density of the available PSInSAR datasets to enable a fair amount of displacement information to be transferred to the sampling grid.

Combining the 50 m grid with Urban Atlas polygons also introduces potential inaccuracies. Assigning a uniform hazard value to entire Urban Atlas polygons, which may be larger than 50 m × 50 m, means that only parts of these polygons might be affected by high hazard, yet the entire polygon is classified with a single value. This is particularly problematic for linear infrastructures, such as roads and railways, where long segments might be classified as at high risk, even if only small portions are actually affected by

significant subsidence hazards. Pixel-based risk assessments exploiting gridded exposure-vulnerability data with spatial resolution similar to that of the PSInSAR-based grid might help to reduce the impact of this spatial discrepancy.

These limitations highlight the need for future studies aimed to incorporate more detailed urban characteristics (i.e., more complete urban vulnerability information and enhanced resolution data) to enable more accurate and reliable subsidence-induced risk assessments.

7. Conclusions

A spatio-temporal analysis of the subsidence patterns and evolution in three of the major cities of Italy between 1992 and 2022 was carried out by exploiting large multi-satellite PSInSAR datasets, highlighting the effectiveness of InSAR techniques to provide crucial information on ground deformation due to land subsidence and other geohazards, and therefore enable the estimation of subsidence-induced hazard and risk.

Vertical displacement rates estimated using PSInSAR reveal the first insight into affected areas within the three selected cities. For Rome, the vertical displacement rates are up to –38 mm/year in critical areas, without any clear decreasing/increasing trend over time, but certainly with a consistent pattern in space. The areas most affected by land subsidence are along the Tiber River alluvium, which gets wider toward the coast, where the Rome–Fiumicino highway is located. Moreover, the angular distortion resulting from differential vertical displacement was computed, acknowledging the significance of this metric in assessing potential infrastructure damage. Categorizing and mapping this value was crucial for a clear interpretation of areas exposed to the risk of structural damage (e.g., fracturing/cracking) across the three cities. Furthermore, computing the β_T over the 30 years of analysis yielded the overall distortion that accumulated in the study areas. In Rome, the most affected areas reach up to 0.2% β_T, which means 0.1 m of vertical displacement over 50 m distances. Finally, the Copernicus Urban Atlas Land Cover/Land Use data were incorporated into the analysis, allowing for better comprehension of the exposure and vulnerability of urban infrastructure. For instance, as affected areas in Rome are mostly critical infrastructure, such as highways and highly dense urban fabric, these were attributed very high to high exposure–vulnerability scores and, in turn, were classified as very-high- or high-risk zones.

In Bologna, the vertical displacement velocity revealed a subsidence velocity of around -55 mm/year before 2000, decreasing to minimums of -25 mm/year by 2022. Through time series analysis, the pattern, some periodicity over time, and recent changes in the land subsidence process were identified. With the angular distortion values, the change in hazard magnitude was also numerically analyzed, for instance, in Bologna the decreasing from values of 0.62 km^2 of high hazard and 11.41 km^2 of medium hazard in the 1990s, to no high hazard and 0.23 km^2 medium hazard for the 2018–2022 period was observed. Particularly in this city, there is a notable change in the role of the primary cause of land subsidence, which can be observed in the generated hazard maps. Whereas groundwater extraction was predominant in the earlier period, it decreased significantly in the following years linking with modified groundwater management strategies, and differential subsidence was observed at more localized sectors, among which highly utilized road infrastructure, such as railway lines.

In Florence, the affected areas were found to be more localized than in the other cities. Vertical displacement rates exhibited peaks of -30 mm/year in the first (1992–2002) and last period analyzed (2018–2022). The maximum total angular distortion reached 0.1%. Despite the relatively lower rates of subsidence compared to Rome and Bologna, Florence featured a substantial number of medium-risk zones due to its dense urban fabric and the persistence in the subsidence processes.

To summarize, the results of this study reveal a notable reduction in subsidence rates over time, accompanied by changes in the distribution of hazard zones within the three cities. This suggests a positive impact of mitigation efforts and highlights the importance

of continued monitoring and understanding of land subsidence dynamics. Furthermore, the identification of specific urban infrastructures affected by subsidence provides valuable insights for targeted interventions and land management strategies. Future research should consider incorporating additional data sources that provide detailed characterization of vulnerability factors to enable a more comprehensive analysis of exposure and assessment of risk.

Author Contributions: Conceptualization, M.L.S. and F.C.; methodology, M.L.S. and F.C.; software, M.L.S.; validation, M.L.S. and F.C.; formal analysis, M.L.S.; investigation, M.L.S.; resources, F.C.; data curation, M.L.S. and F.C.; writing—original draft preparation, M.L.S. and F.C.; writing—review and editing, C.A.F.; visualization, M.L.S.; supervision, F.C.; project administration, F.C.; funding acquisition, M.L.S., C.A.F. and F.C. All authors have read and agreed to the published version of the manuscript.

Funding: This research was carried out in the framework of the research internship of Ms M. Lenardón Sánchez and Ms C. A. Farías at the National Research Council—Institute of Atmospheric Sciences and Climate (CNR-ISAC) in Rome, Italy, under the supervision of F. Cigna, as part of the University of Pavia's Modulo ASI Scholarships Programme 2024. Funding to Dr F. Cigna was provided via the European Union—Next Generation EU, Mission 4—Component 2 (M4C2), PRIN 2022 PNRR project SubRISK+ 2023–2025 (CUP B53D23033400001).

Data Availability Statement: This publication has been prepared using European Union's Copernicus Land Monitoring Service information; https://doi.org/10.2909/fb4dffa1-6ceb-4cc0-8372-1ed354c285e6 (Urban Atlas 2018), https://doi.org/10.2909/d92e61be-d6e8-4bc1-aa10-f742bf27bab9 (EGMS L2b, Calibrated). InSAR datasets are available via EGMS Explorer at: https://egms.land.copernicus.eu/ (accessed on 1 April 2024). Geological datasets for Rome are distributed by Lazio Region at: http://dati.lazio.it/catalog/it/dataset/carta-geologica-informatizzata-regione-lazio-25000 (accessed on 1 April 2024), while the Italian Landslide Inventory (IFFI) is available at: https://idrogeo.isprambiente.it/app/iffi (accessed on 1 April 2024).

Acknowledgments: Google satellite imagery, Copyright ©2024 Google.

Conflicts of Interest: The authors declare no conflicts of interest. The funders had no role in the design of the study; in the collection, analyses, or interpretation of data; in the writing of the manuscript; or in the decision to publish the results.

Appendix A

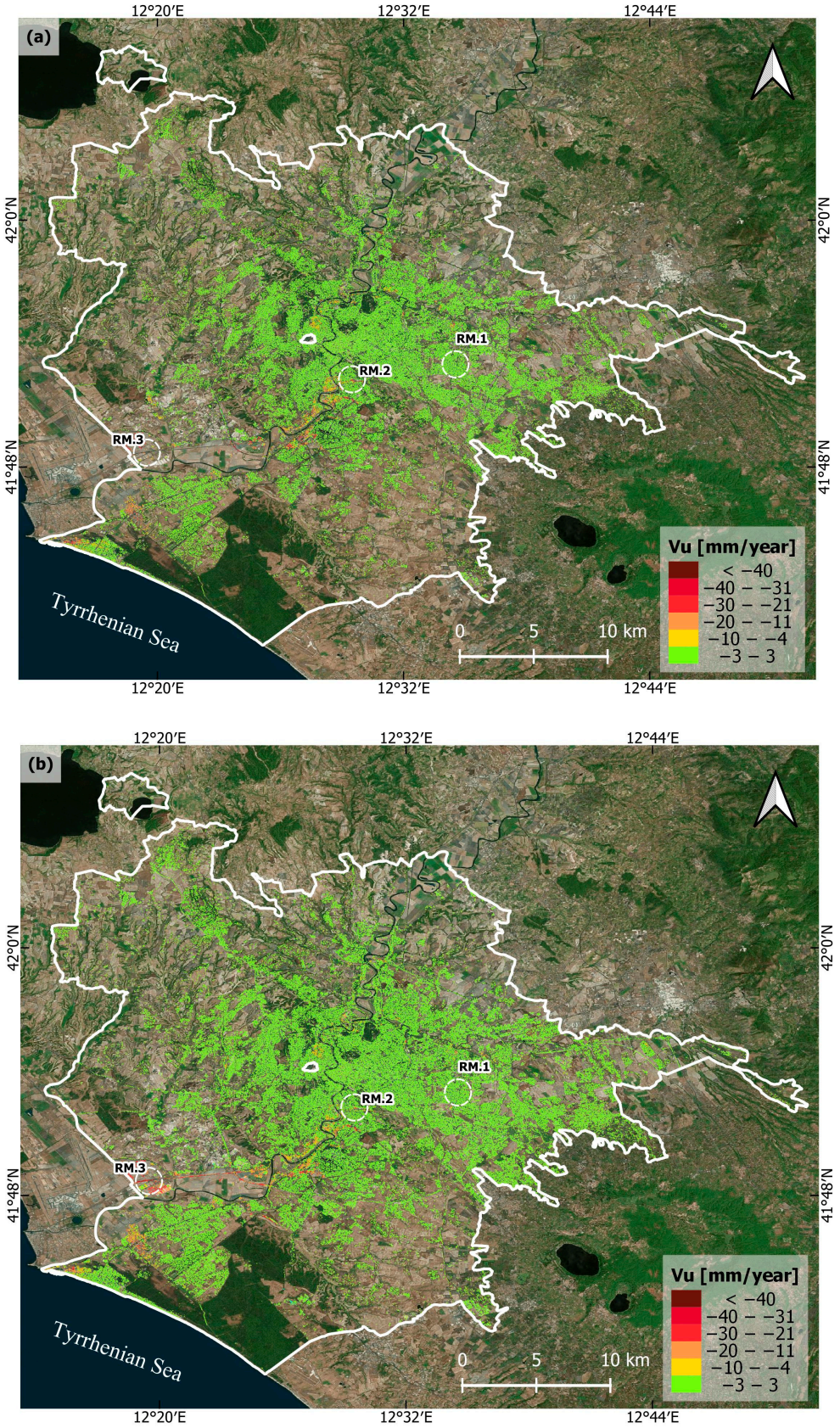

Figure A1. *Cont.*

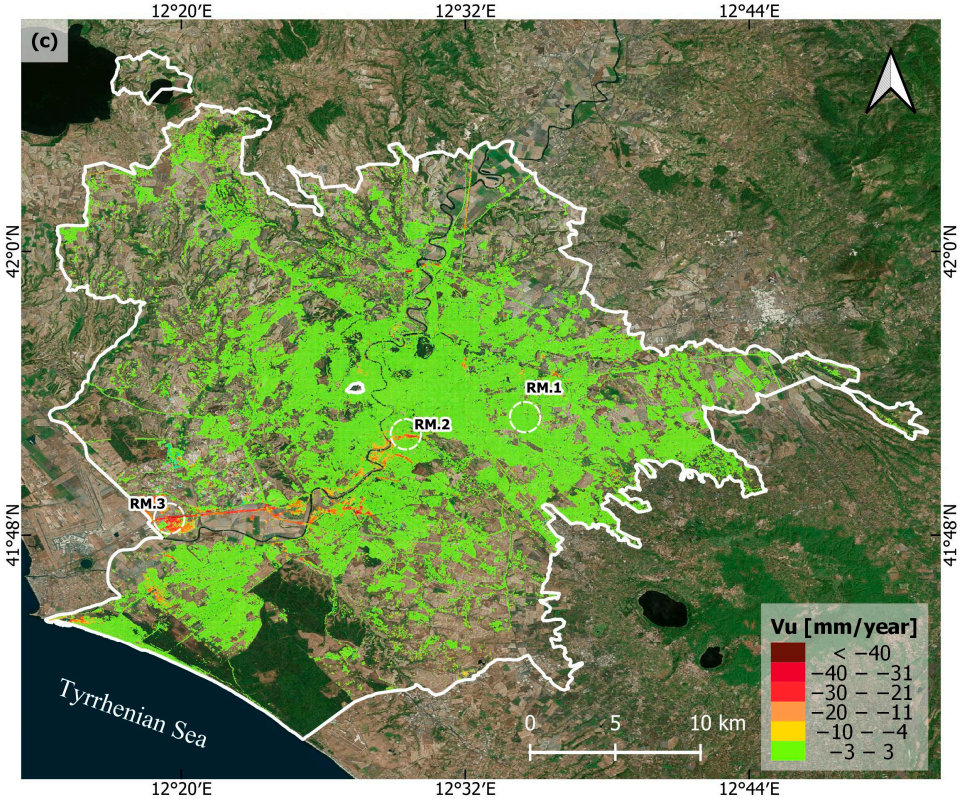

Figure A1. Vertical displacement velocities of Rome in: (**a**) 1992–2000 (ERS-1/2 datasets), (**b**) 2002–2010 (ENVISAT datasets), and (**c**) 2013–2014 (COSMO-SkyMed dataset). PSInSAR data are overlapped onto Google Earth imagery.

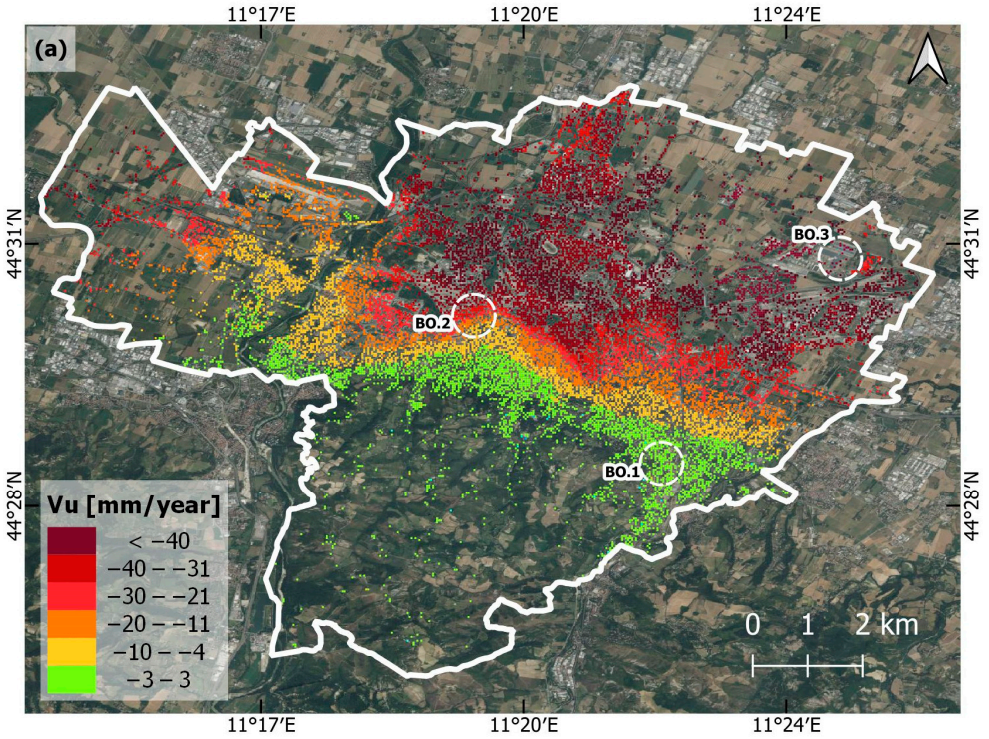

Figure A2. *Cont.*

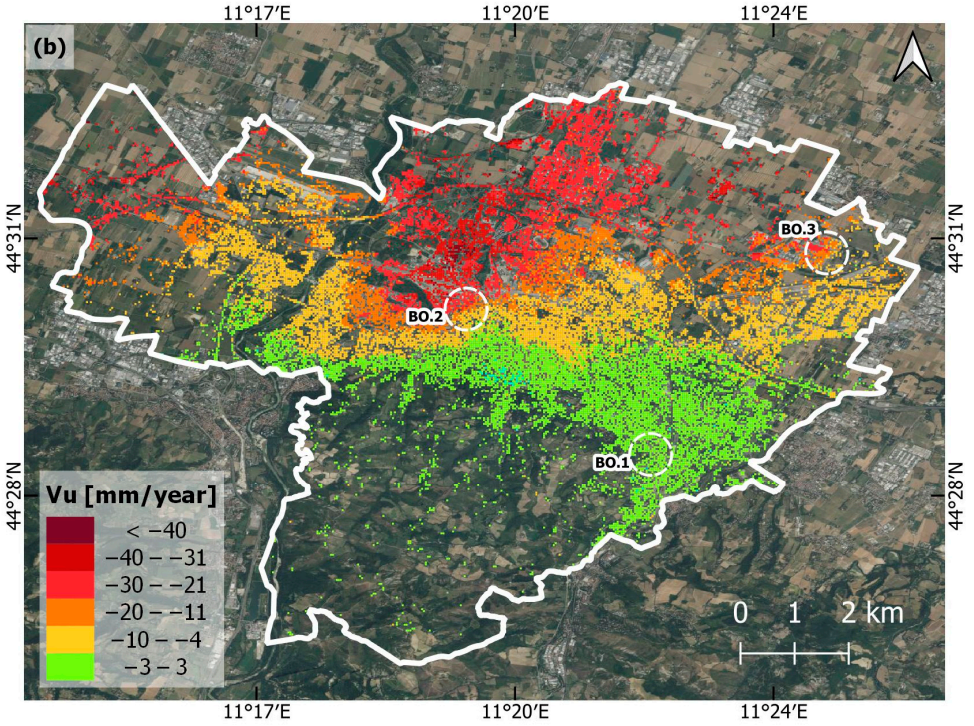

Figure A2. Vertical displacement velocities of Bologna in: (**a**) 1992–2000 (ERS-1/2 datasets), and (**b**) 2002–2010 (ENVISAT datasets). PSInSAR data are overlapped onto Google Earth imagery.

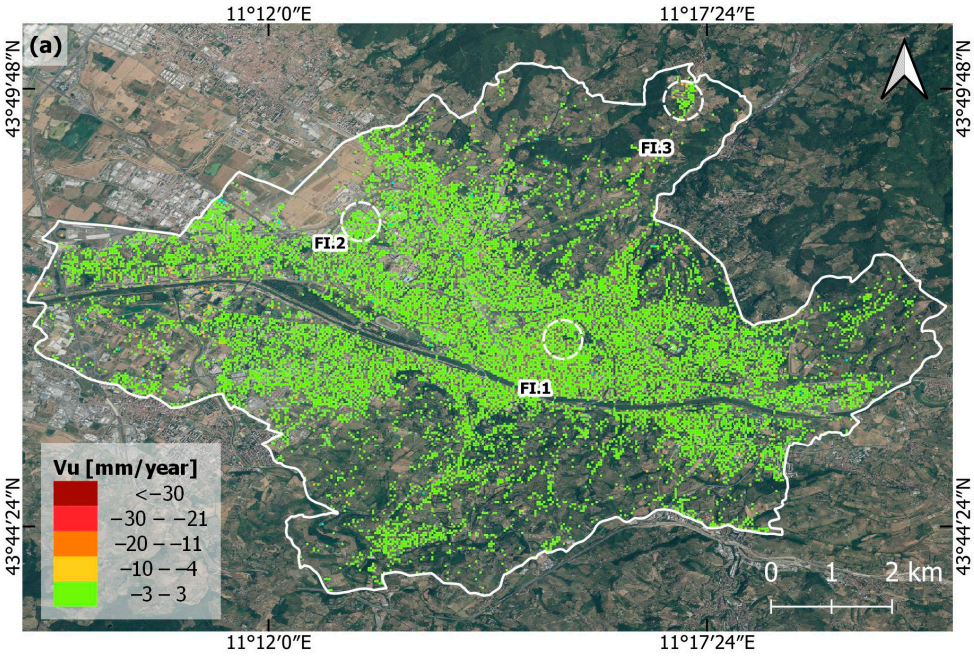

Figure A3. *Cont.*

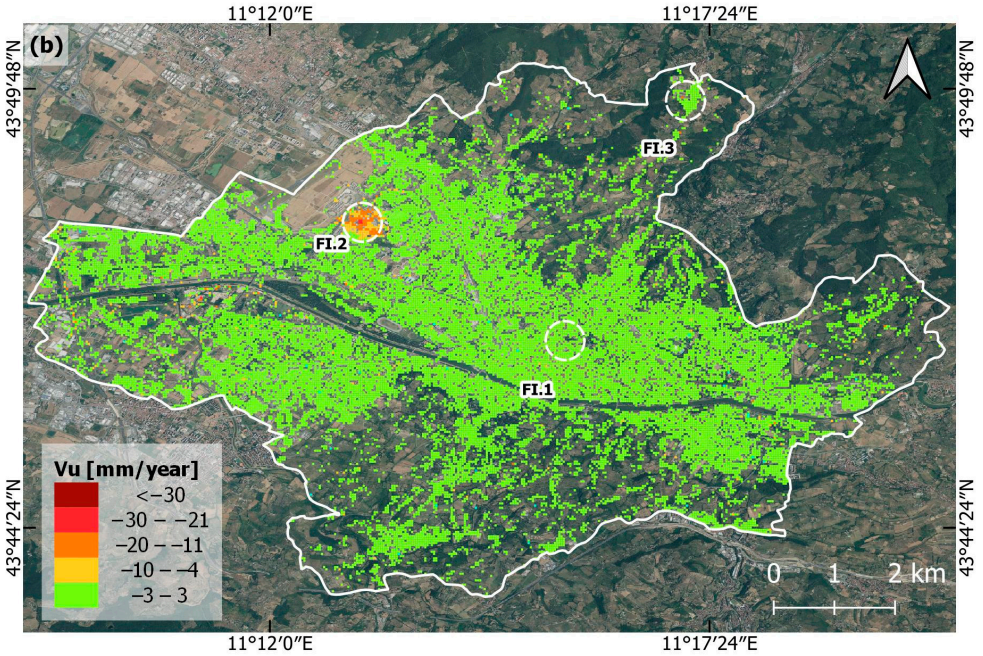

Figure A3. Vertical displacement velocities of Florence in: (**a**) 1992–2000 (ERS-1/2 datasets), and (**b**) 2002–2010 (ENVISAT datasets). PSInSAR data are overlapped onto Google Earth imagery.

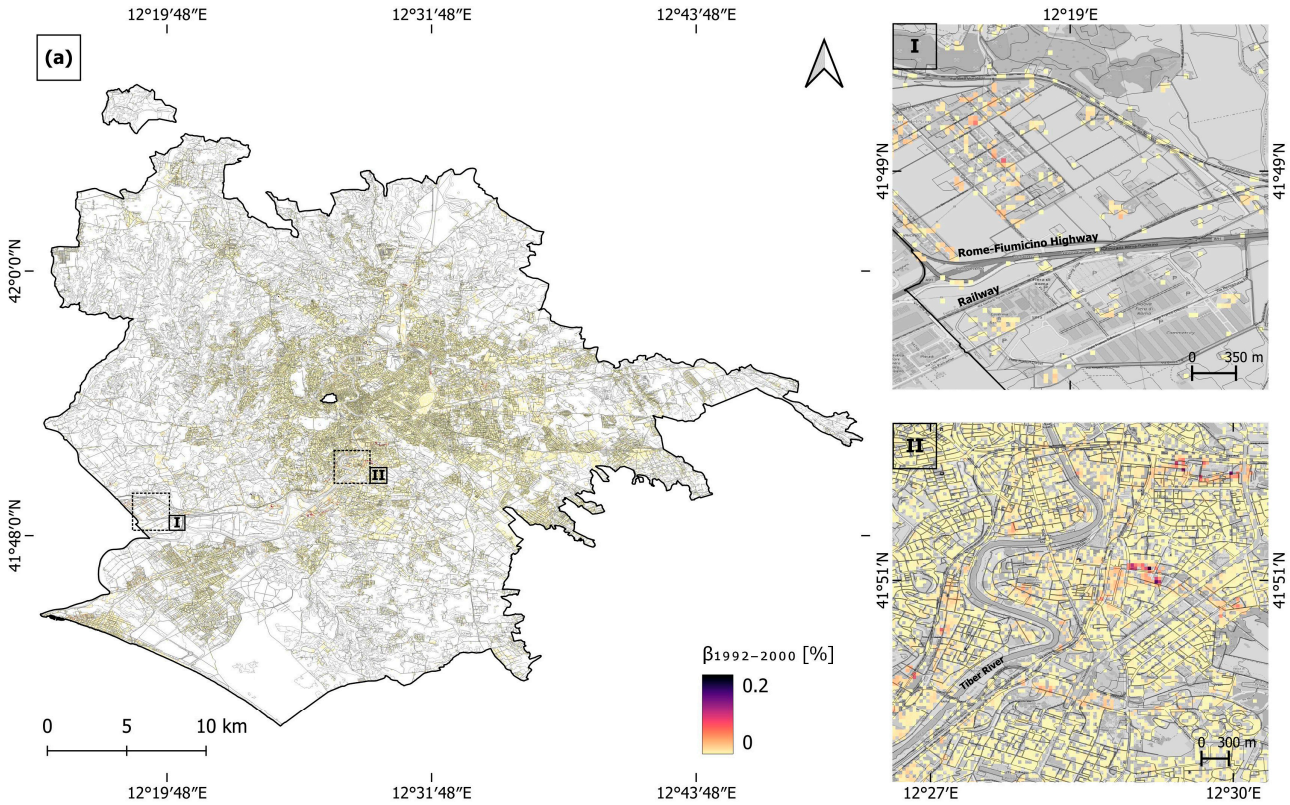

Figure A4. *Cont.*

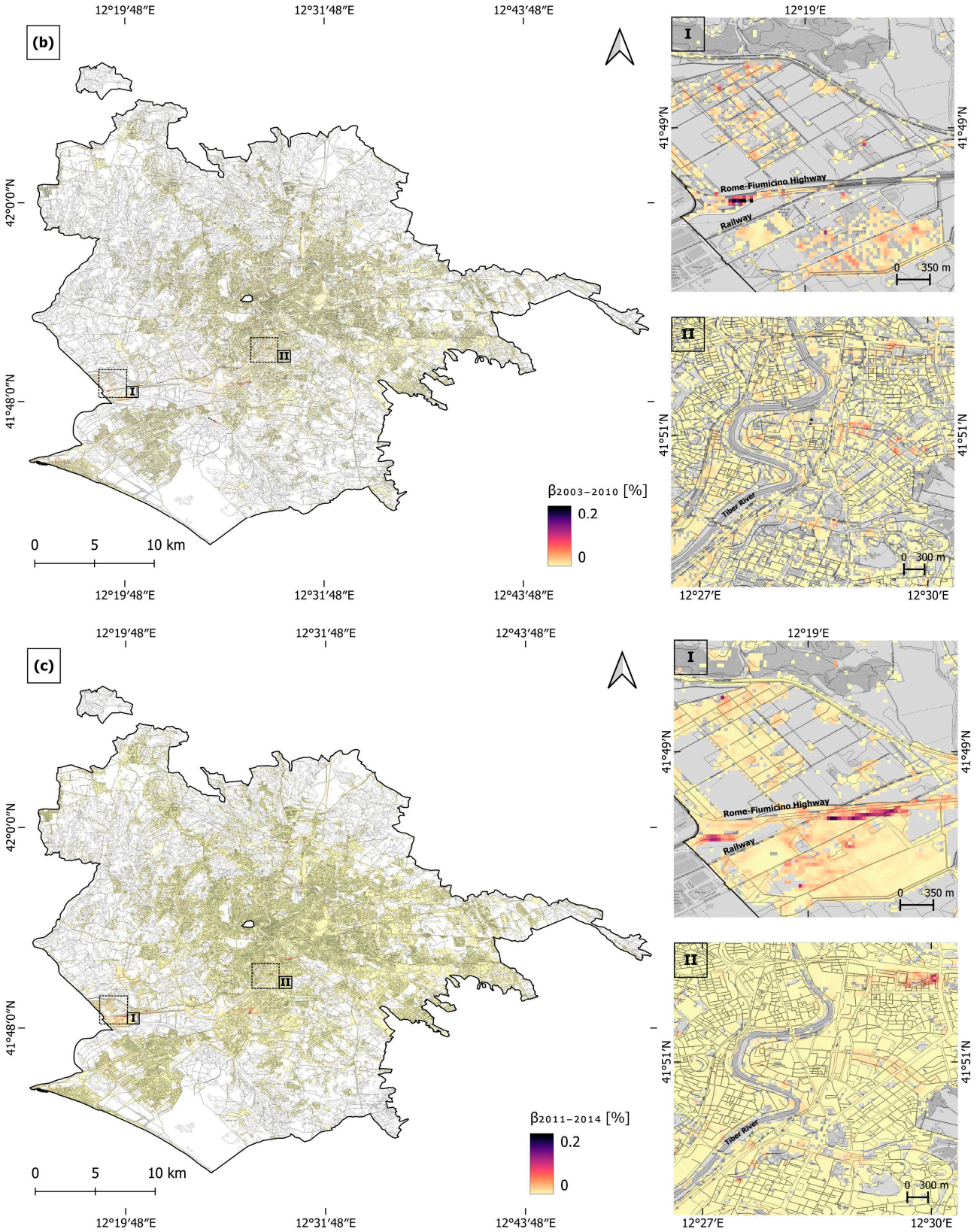

Figure A4. Rome hazard maps, representing (**a**) the 1992–2000 period angular distortion, $\beta_{1992–2000}$, (**b**) the 2003–2010 period angular distortion, $\beta_{2003–2010}$, and (**c**) the 2011–2014 period angular distortion, $\beta_{2011–2014}$. The 2018 Urban Atlas layer is superimposed and zooms (I) and (II) are overlapped onto the OpenStreetMap on grey scale.

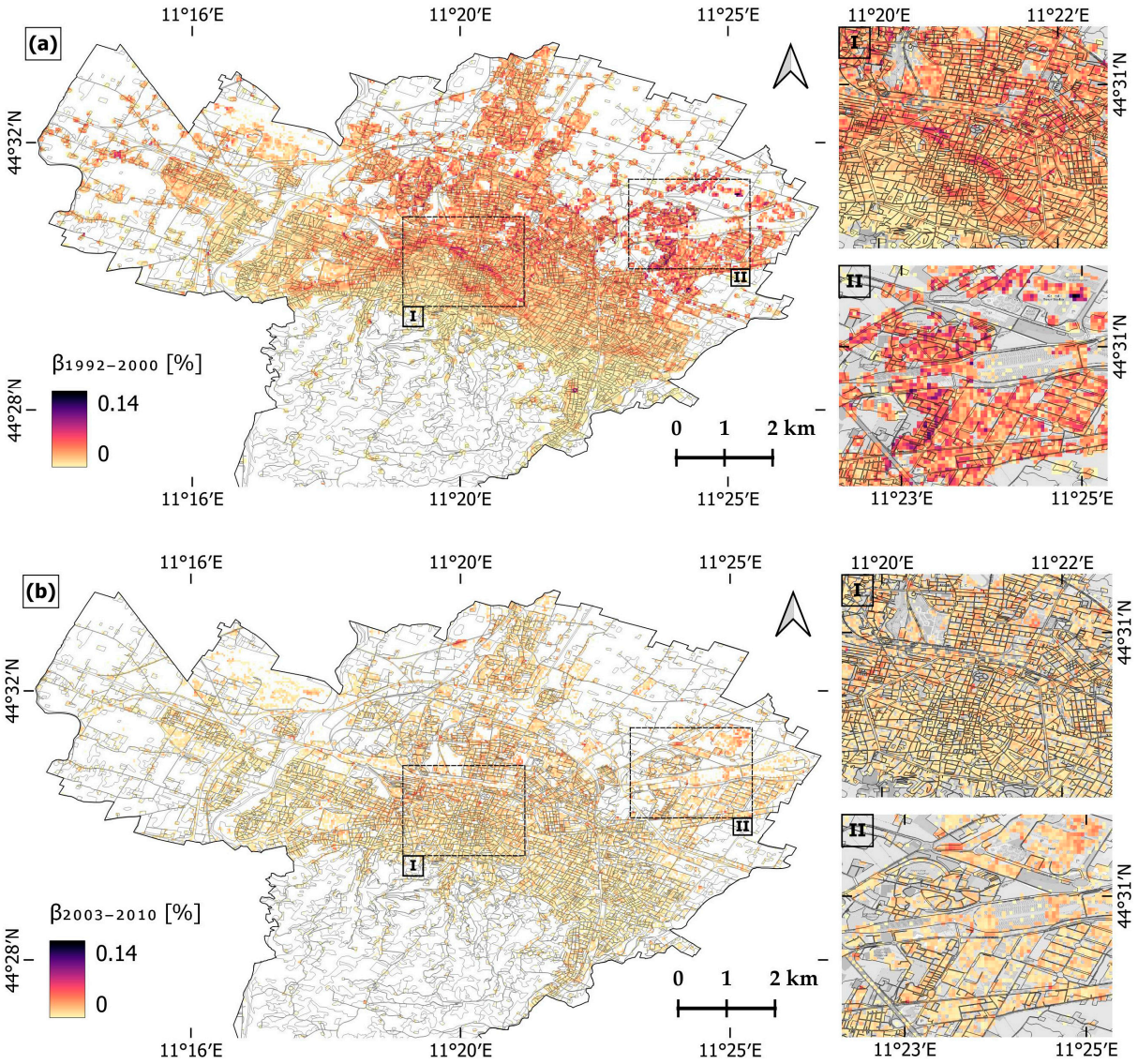

Figure A5. Bologna hazard maps, representing (**a**) the 1992–2000 period angular distortion, $\beta_{1992–2000}$ and (**b**) the 2003–2010 period angular distortion, $\beta_{2003–2010}$. The 2018 Urban Atlas layer is superimposed and zooms (I) and (II) are overlapped onto the OpenStreetMap on grey scale.

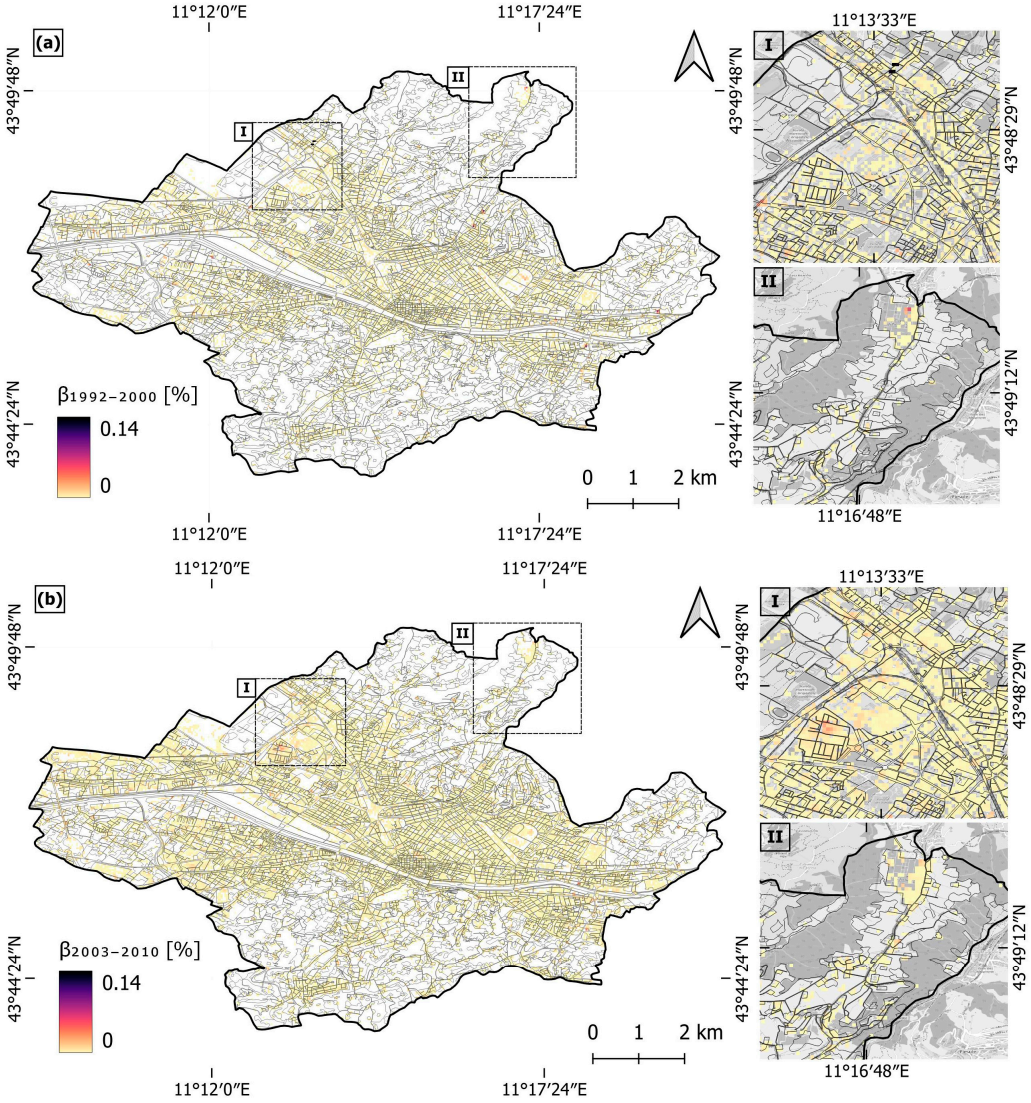

Figure A6. Florence hazard maps, representing (**a**) the 1992–2000 period angular distortion, $\beta_{1992–2000}$ and (**b**) the 2003–2010 period angular distortion, $\beta_{2003–2010}$. The 2018 Urban Atlas layer is superimposed and zooms (I) and (II) are overlapped onto the OpenStreetMap on grey scale.

References

1. Scheer, D.; Benighaus, C.; Benighaus, L.; Renn, O.; Gold, S.; Röder, B.; Böl, G. The Distinction Between Risk and Hazard: Understanding and Use in Stakeholder Communication. *Risk Anal.* **2014**, *34*, 1270–1285. [CrossRef] [PubMed]
2. Van Westen, C.J. Remote Sensing and Geographic Information Systems for Natural Disaster Management. *Environ. Model. GIS Remote Sens.* **2002**, *6*, 200–226.
3. Herrera-García, G.; Ezquerro, P.; Tomás, R.; Béjar-Pizarro, M.; López-Vinielles, J.; Rossi, M.; Mateos, R.M.; Carreón-Freyre, D.; Lambert, J.; Teatini, P.; et al. Mapping the global threat of land subsidence. *Science* **2021**, *371*, 34–36. [CrossRef]
4. Zhang, Y.; Huang, H.; Liu, Y.; Liu, Y. Self-weight consolidation and compaction of sediment in the Yellow River Delta, China. *Phys. Geogr.* **2018**, *39*, 84–98. [CrossRef]
5. Poland, J.F. *Guidebook to Studies of Land Subsidence due to Ground-Water Withdrawal*; UNESCO: Paris, France, 1984.
6. Galloway, D.L.; Burbey, T.J. Review: Regional land subsidence accompanying groundwater extraction. *Hydrogeol. J.* **2011**, *19*, 1459–1486. [CrossRef]
7. Holzer, T.L.; Johnson, A.I. Land subsidence caused by ground water withdrawal in urban areas. *GeoJournal* **1985**, *11*, 245–255. [CrossRef]
8. Wang, Z.-F.; Cheng, W.-C.; Wang, Y.-Q. Investigation into geohazards during urbanization process of Xi'an, China. *Nat. Hazards* **2018**, *92*, 1937–1953. [CrossRef]
9. Cigna, F.; Tapete, D. Urban growth and land subsidence: Multi-decadal investigation using human settlement data and satellite InSAR in Morelia, Mexico. *Sci. Total Environ.* **2022**, *811*, 152211. [CrossRef]
10. Holzer, T.L.; Pampeyan, E.H. Earth Fissures and Localized Differential Subsidence. *Water Resour. Res.* **1981**, *17*, 223–227. [CrossRef]

11. Navarro-Hernández, M.I.; Valdes-Abellan, J.; Tomás, R.; Tessitore, S.; Ezquerro, P.; Herrera, G. Analysing the Impact of Land Subsidence on the Flooding Risk: Evaluation Through InSAR and Modelling. *Water Resour. Manag.* **2023**, *37*, 4363–4383. [CrossRef]
12. Rosen, P.A.; Hensley, S.; Joughin, I.R.; Li, F.K.; Madsen, S.N.; Rodriguez, E.; Goldstein, R.M. Synthetic aperture radar interferometry. *Proc. IEEE* **2000**, *88*, 333–380. [CrossRef]
13. Raspini, F.; Caleca, F.; Del Soldato, M.; Festa, D.; Confuorto, P.; Bianchini, S. Review of satellite radar interferometry for subsidence analysis. *Earth-Sci. Rev.* **2022**, *235*, 104239. [CrossRef]
14. Quin, G.; Loreaux, P. Submillimeter accuracy of multipass corner reflector monitoring by PS technique. *IEEE Trans. Geosci. Remote Sens.* **2013**, *51*, 1775–1783. [CrossRef]
15. Cigna, F.; Esquivel Ramírez, R.; Tapete, D. Accuracy of Sentinel-1 PSI and SBAS InSAR displacement velocities against GNSS and geodetic leveling monitoring data. *Remote Sens.* **2021**, *13*, 4800. [CrossRef]
16. Cigna, F.; Tapete, D. Satellite InSAR survey of structurally-controlled land subsidence due to groundwater exploitation in the Aguascalientes Valley, Mexico. *Remote Sens. Env.* **2021**, *254*, 112254. [CrossRef]
17. Cigna, F.; Tapete, D. Present-day land subsidence rates, surface faulting hazard and risk in Mexico City with 2014–2020 Sentinel-1 IW InSAR. *Remote Sens. Environ.* **2021**, *253*, 112161. [CrossRef]
18. Ohenhen, L.O.; Shirzaei, M. Land Subsidence Hazard and Building Collapse Risk in the Coastal City of Lagos, West Arica. *Earths Future* **2022**, *10*, e2022EF003219. [CrossRef]
19. Garg, S.; Motagh, M.; Indu, J.; Karanam, V. Tracking hidden crisis in India's capital from space: Implications of unsustainable groundwater use. *Sci. Rep.* **2022**, *12*, 651. [CrossRef]
20. Cecconi, M.; Scarapazzi, M.; Viggiani, G.M.B. On the geology and the geotechnical properties of pyroclastic flow deposits of the Colli Albani. *Bull. Eng. Geol. Environ.* **2010**, *69*, 185–206. [CrossRef]
21. Stramondo, S.; Bozzano, F.; Marra, F.; Wegmuller, U.; Cinti, F.R.; Moro, M.; Saroli, M. Subsidence induced by urbanisation in the city of Rome detected by advanced InSAR technique and geotechnical investigations. *Remote Sens. Environ.* **2008**, *112*, 3160–3172. [CrossRef]
22. Elmi, C.; Bergonzoni, A.; Massa, T.; Montaletti, V.; Baratella, P.L.; Ronchi, A. Il territorio di pianura del Comune di Bologna: Aspetti geologic e geotechnici. *G. Geol.* **1984**, *46*, 127–152.
23. Zuccarini, A.; Giacomelli, S.; Severi, P.; Berti, M. Long-term spatiotemporal evolution of land subsidence in the urban area of Bologna, Italy. *Bull. Eng. Geol. Environ.* **2024**, *83*, 35. [CrossRef]
24. European Environment Agency. *Urban Atlas Land Cover/Land Use 2018 (Vector), Europe, 6-Yearly*; EEA: Copenhagen, Denmark, 2021. [CrossRef]
25. European Environment Agency. Urban Atlas 2018: Copernicus Land Monitoring Service. Copernicus. Available online: https://land.copernicus.eu/en/products/urban-atlas/urban-atlas-2018 (accessed on 1 April 2024).
26. Kotzerke, P.; Siegmund, R.; Langenwalter, J. End-to-End Implementation and Operation of the European Ground Motion Service (EGMS). In *Product User Manual*; report no. EGMS-D4-PUM-SC1-2.0-007, v.1.6; EEA: Copenhagen, Denmark, 2022; p. 56.
27. Costantini, M.; Minati, F.; Ciminelli, M.G.; Ferretti, A.; Novali, F.; Costabile, S. SAR interferometry analysis of very large areas: Results over the entire Italian territory. In Proceedings of the IEEE International Geoscience and Remote Sensing Symposium (IGARSS), Beijing, China, 10–15 July 2016; pp. 2070–2073. [CrossRef]
28. Cigna, F.; Tapete, D.; Garduño-Monroy, V.H.; Muñiz-Jauregui, J.A.; García-Hernández, O.H.; Jiménez-Haro, A. Wide-area InSAR survey of surface deformation in urban areas and geothermal fields in the eastern Trans-Mexican Volcanic Belt, Mexico. *Remote Sens.* **2019**, *11*, 2341. [CrossRef]
29. Skempton, A.W.; Macdonald, D.H. The allowable settlements of buildings. *Proc. Inst. Civ. Eng.* **1956**, *5*, 727–768. [CrossRef]
30. Burland, J.B.; Wroth, C.P. *Settlement of Buildings and Associated Damage*; Building Research Establishment: Garston, UK, 1975.
31. Sanabria, M.P.; Guardiola-Albert, C.; Tomás, R.; Herrera, G.; Prieto, A.; Sánchez, H.; Tessitore, S. Subsidence activity maps derived from DInSAR data: Orihuela case study. *Nat. Hazards Earth Syst. Sci.* **2014**, *14*, 1341–1360. [CrossRef]
32. Vassileva, M.; Al-Halbouni, D.; Motagh, M.; Walter, T.R.; Dahm, T.; Wetzel, H.-U. A decade-long silent ground subsidence hazard culminating in a metropolitan disaster in Maceió, Brazil. *Sci. Rep.* **2021**, *11*, 7704. [CrossRef]
33. Ohenhen, L.O.; Shirzaei, M.; Barnard, P.L. Slowly but surely: Exposure of communities and infrastructure to subsidence on the US east coast. *PNAS Nexus* **2024**, *3*, pgad426. [CrossRef]
34. Delgado Blasco, J.M.; Foumelis, M.; Stewart, C.; Hooper, A. Measuring urban subsidence in the Rome Metropolitan Area (Italy) with Sentinel-1 SNAP-StaMPS Persistent Scatterer Interferometry. *Remote Sens.* **2019**, *11*, 129. [CrossRef]
35. Manunta, M.; Marsella, M.; Zeni, G.; Sciotti, M.; Atzori, S.; Lanari, R. Two-scale surface deformation analysis using the SBAS-DInSAR technique: A case study of the city of Rome, Italy. *Int. J. Remote Sens.* **2008**, *29*, 1665–1684. [CrossRef]
36. Pratesi, F.; Tapete, D.; Del Ventisette, C.; Moretti, S. Mapping interactions between geology, subsurface resource exploitation and urban development in transforming cities using InSAR Persistent Scatterers: Two decades of change in Florence, Italy. *Appl. Geogr.* **2016**, *77*, 20–37. [CrossRef]

37. Giacomelli, S.; Zuccarini, A.; Amorosi, A.; Bruno, L.; Di Paola, G.; Martini, A.; Severi, P.; Berti, M. 3D geological modelling of the Bologna urban area (Italy). *Eng. Geol.* **2023**, *324*, 107242. [CrossRef]
38. Farías, C.A.; Lenardón Sánchez, M.; Bonì, R.; Cigna, F. Statistical and Independent Component Analysis of Sentinel-1 InSAR Time Series to Assess Land Subsidence Trends. *Remote Sens.* **2024**, *16*, 4066. [CrossRef]